Cell Reports

Article

Evolution of a melanoma that escapes allogeneic rejection

Graphical abstract

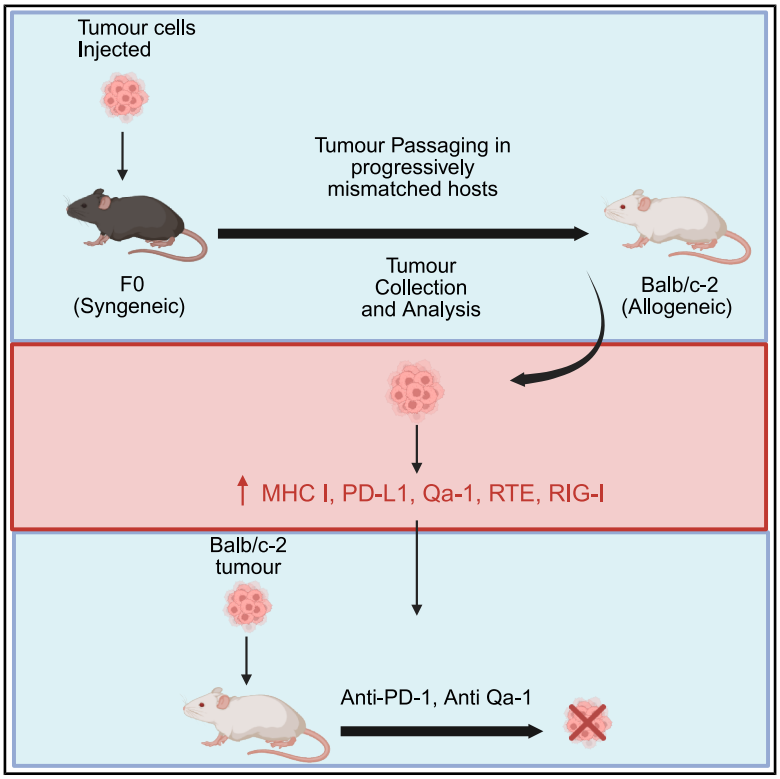

Highlights

- Here, a mouse melanoma was adapted to escape mismatched histocompatibility barriers
- The transplantable melanoma showed an antiviral immune signature
- Blocking PD-L1 and Qa-1 led to rejection of the transplantable melanoma in mice
- Similar immune signatures seen in human melanomas responsive to PD-1 blockade

Authors

Ahmed Rokan, Mariana O. Diniz, Jose I. de las Heras, ..., Maria Secrier, George Kassiotis, Ariberto Fassati

Correspondence

a.fassati@ucl.ac.uk

In brief

Rokan et al. evolved mouse melanoma to bypass immune barriers, making it transplantable. Transplantable tumors activated antiviral signals and blocked immune attack. Similar traits appear in some human melanomas, helping us understand how cancer evades immune detection and the histocompatibility barrier.

Rokan et al., 2025, Cell Reports *44*, 116288
September 23, 2025 © 2025 The Authors. Published by Elsevier Inc.
https://doi.org/10.1016/j.celrep.2025.116288

CellPress

Cell Reports

CellPress
OPEN ACCESS

Article

Evolution of a melanoma that escapes allogeneic rejection

Ahmed Rokan,[1,2] Mariana O. Diniz,[1] Jose I. de las Heras,[3] Callum Hall,[4] Somaya Noorsaeed,[2,5] Clare L. Bennett,[6] Maria Secrier,[7] George Kassiotis,[4] and Ariberto Fassati[2,8,*]

[1]Department of Medical Laboratory Sciences, College of Applied Medical Sciences, Prince Sattam Bin Abdulaziz University, Alkharj 11942, Saudi Arabia

[2]Division of Infection & Immunity and Institute of Immunity and Transplantation, The Pears Building, University College London, Pond Street, London NW3 2PP, UK

[3]Institute of Cell Biology, School of Biological Sciences, the University of Edinburgh, the Swann Building, Max Born Crescent, Edinburgh EH9 3BF, UK

[4]The Francis Crick Institute, 1 Midland Road, London NW1 1AT, UK

[5]Department of Medical Laboratory Sciences, Faculty of Applied Medical Sciences, King Abdulaziz University, Jeddah, 22254 Saudi Arabia

[6]Department of Haematology, UCL Cancer Institute, Paul O'Gorman Building, 72 Huntley Street, London WC1E 6DD, UK

[7]UCL Genetics Institute, Department of Genetics, Evolution and Environment, University College London, Darwin Building, Gower Street, London WC1E 6BT, UK

[8]Lead contact

*Correspondence: a.fassati@ucl.ac.uk

https://doi.org/10.1016/j.celrep.2025.116288

SUMMARY

The histocompatibility barrier prevents the transfer of both normal and tumor cells between individuals; however, clonally transmissible cancers in dogs, Tasmanian devils, and soft-shell clams can naturally transmit as allografts. To understand if cancer cells can more generally evolve to escape the histocompatibility barrier, we have serially passaged a mouse melanoma into increasingly mismatched mouse strains until a transplantable tumor emerged. The transplantable melanoma cells are characterized by an antiviral immune signature and the upregulation of endogenous retrotransposable elements (RTEs), major histocompatibility complex class I (MHC class I), programmed cell death ligand-1 (PD-L1), and Qa-1 non-classical MHC molecules. Knockout of the RNA sensor retinoic acid-inducible gene I (RIG-I) reduces expression of PD-L1 and Qa-1, and antibody-mediated blockade of PD-L1 and Qa-1 induces tumor rejection. Thus, an immune antiviral signature linked to RTEs upregulation facilitates escape of the melanoma from allogeneic rejection, simultaneously making the tumor sensitive to PD-L1 and Qa-1 antagonism. A similar immune signature is found in human melanomas that respond to PD-L1 blockade.

INTRODUCTION

Early tumor transplantation experiments demonstrated that cancer cells could not be transplanted between different mouse strains, and that this transplantation barrier had a Mendelian inheritance pattern.[1,2] Snell, Dausset, Benacerraff, and others identified the major histocompatibility complex (MHC) as a central component of the barrier to transplantation, called the histocompatibility barrier.[3] Because the MHC is highly polymorphic and ubiquitously expressed, cells from different individuals (allografts) are recognized as non-self and rejected, mainly by T lymphocytes, although monocytes, natural killer (NK), and B lymphocytes can also contribute.[4] Additional polymorphic molecules, called minor histocompatibility antigens and not related to MHC, can also promote T cell-mediated allograft rejection.[5]

The histocompatibility barrier is challenged by clonally transmissible cancers, which are allografts spreading naturally in dogs (the canine venereal transmissible tumor or CTVT), Tasmanian devils (the devil facial tumor disease or DFTD), and soft-shell clams.[6] Thus, at least in rare instances, tumors are able to evolve naturally the capacity to escape allogeneic rejection. This notion is supported by rare cases described in the literature of accidental heterologous transplantation of cancer in otherwise healthy individuals,[7,8] and by the transmission in pregnancy of gestational choriocarcinoma, a hemi-allograft derived from placental trophoblasts that expresses both maternal and fetal antigens.[9]

The fundamental question, therefore, arises whether cancer can evolve more broadly to escape allogeneic rejection, and how this is achieved. The implications are significant and may help to understand the limits of the allogeneic barrier in cancer and what mechanisms may lead to the extreme forms of tumor immune evasion.

Archival samples going back to the founder tumors are not available for CTVT, DFT1, or DFT2, which limits our understanding of how cancer may adapt to escape the histocompatibility barrier. Therefore, new experimental models that recapitulate the evolution of transplantable and transmissible cancers, allowing their systematic analysis, are required.

This is an open access article under the CC BY license (http://creativecommons.org/licenses/by/4.0/).

Table 1. Tumor passages and accepted transplants

Recipient mouse strain	Tumor passage	No. of injected mice	No. of "takes" (tumors that grew in 2 weeks)	No. of tumors dissociated
C57BL/6	F0	17	16	9
F1 (C57BL/6 × BALB/c)	F1	13	12	9
F2 (F1 × F1)	F2	17	16	5
N2 (F2 × BALB/c)	N2.1	15	6	6
N2	N2.2	30	14	3
N2	N2.3	6	6	3
BALB/c	Balb/c-1	12	9	5
BALB/c	Balb/c-2	16	15	5
C57BL/6	B6	6	6	4
CBA/Ca	CBA/Ca	10	10	4
FVB/N	FVB/N	10	10	4
N2	YUMM1.7	10	0	0
BALB/c	YUMM1.7	20	0	0

See also Figures S1–S4.

Inbred mouse strains have well-characterized major and minor histocompatibility antigens haplotypes and are widely used to study mechanisms of transplant rejection and tolerance.[10] Remarkably, mouse transplantation studies in the 1920s reported the odd emergence of tumors that were transplantable in adult immunocompetent hosts across different inbred strains.[11,12] Similar results were reported by Barrett and Deringer in 1952,[13] although at the time, no molecular characterization of the tumors could be performed, preventing any firm conclusions. More recently, an *in vivo* serial passaging approach in syngeneic mice selected melanomas that evolved full resistance to combined immune checkpoint therapy.[14] Together, these studies indicate that experimental models based on the *in vivo* selection of tumor cells by serial passaging can be used to discover mechanisms of resistance of cancer to immune responses.

We have therefore employed this experimental approach using a well-characterized primary mouse melanoma that shares key features with human melanoma, and serially passaged tumor cells into progressively more mismatched, fully immunocompetent mouse strains until we obtained a tumor that was allotransplantable. We then analyzed the sequential tumor passages to understand the molecular mechanisms leading to the escape from allogeneic rejection. We found that tumor escape from allogeneic rejection developed simultaneously with an antiviral immune signature, the dysregulation of RTEs, and the upregulation of interferon (IFN)-induced immune protective molecules PD-L1 and Qa-1, a non-classical MHC. Thus, our model revealed mechanisms of cancer escape from strong immune selection and showed that cancer more broadly can evolve to escape allogeneic rejection.

RESULTS

To select the best conditions for evolving a transplantable tumor, we adapted the passaging strategy of older tumor transplantation studies[11,13] and used genetic information on CTVT, which was shown to be transcriptionally similar to melanoma[15] and to have deletions of *Cdkn2a* and *Pten*.[16] Hence, we used the YUMM1.7 (Yale University mouse melanoma) cells, which were derived from a male $Braf^{V600E}$, $Cdkn2a^{-/-}$, $Pten^{-/-}$ C57BL/6J mouse[17]; these melanoma cells form tumors when injected into syngeneic mice, are not very immunogenic, and do not respond to anti-CTLA4 and anti-PD-1 antibodies,[18] but express detectable levels of MHC-I.[19] Furthermore, these cells are clinically relevant because genetic mutations in *PTEN* and *BRAF* are present in 50% of human melanomas, 70%–88% of which are BrafV600E.[20]

To optimize the experiments, 1×10^5 or 1×10^6 YUMM1.7 cells were injected subcutaneously into the left flank of male and female C57BL/6 mice, and tumor growth and mouse weight were monitored at regular intervals. Injection of 1×10^6 cells resulted in 100% (5/5) tumor growth within 1 week, whereas injection of 1×10^5 cells resulted in 80% (4/5) tumor growth with a slower kinetic (Figure S1A). No weight loss was observed at any of the tested conditions (Figure S1B). Therefore, all subsequent experiments were conducted with 1×10^6 YUMM1.7 cells.

To adapt YUMM1.7 tumors escape allogeneic rejection, the following inbred mouse strains and their hybrids were selected: C57BL/6 (MHC haplotype H-$2K^b$ H-$2D^b$ H-$2L^{null}$ I-A^b I-E^{null}), BALB/c (haplotype H-$2K^d$ H-$2D^d$ H-$2L^d$ I-A^d I-E^d), F1 generation (C57BL/6 × BALB/c), F2 generation (F1 × F1), N2 generation (F2 x BALB/c), CBA/Ca haplotype (H-$2K^k$ H-$2D^k$ H-$2L^{null}$ I-A^k I-E^k), and FVB/N (haplotype H-$2K^q$ H-$2D^q$ H-$2L^q$ I-A^q I-E^{null}). Thus, except for C57BL/6 mice, which were syngeneic, the other inbred strains were mismatched relative to YUMM1.7 cells for MHC-I and MHC-II molecules.[21] The tumor passaging steps were as follows: C57BL/6 (F0) followed by F1 hybrid, then F2 hybrid followed by N2 hybrid, followed by BALB/c and then CBA and FVB/N (Figure S2A). The tumor passaging was repeated three times in the N2 hybrid (hereafter referred to as the N2.1, N2.2, and N2.3 tumors) and twice in the BALB/c mice (hereafter referred to as Balb/c-1 and Balb/c-2 tumors) to help adaptation to the mismatched host. The Balb/c-2 tumor cells were also injected into C57BL/6 mice to confirm that passaging did not alter their transplantation potential into the parental strain (Figure S2A). At each passage, mice were observed daily for up to 3 weeks. Tumors that progressively grew within 2 weeks after injection were classified as accepted grafts or "takes" and were harvested and dissociated. Genotyping confirmed that cells from each passage were all C57BL/6J and, as expected for YUMM1.7 cells, contained the *Cre* recombinase gene[17] (Table S1).

Freshly dissociated tumors were analyzed by multiparameter flow cytometry, whereas tumor cells were analyzed following *in vitro* cultures by RNA sequencing (RNA-seq) and flow cytometry. Some tumors were not dissociated and were instead collected for bulk RNA-seq (Figure S2B). The cells dissociated from the largest tumors were expanded *in vitro* for 2–4 passages and injected into the next mouse strain or hybrid. Two tumor lines were taken forward from the F0 to the N2.1 passage, but one of these two lines was lost at the N2.2 passage. From this single N.2.2 line, two new lines were generated and taken forward (Figure S3).

There was a high proportion of takes in syngeneic F0 mice, and in F1 mice, which express both parental MHC haplotypes and can therefore accept grafts from either parent[22] (Table 1).

CellPress
OPEN ACCESS

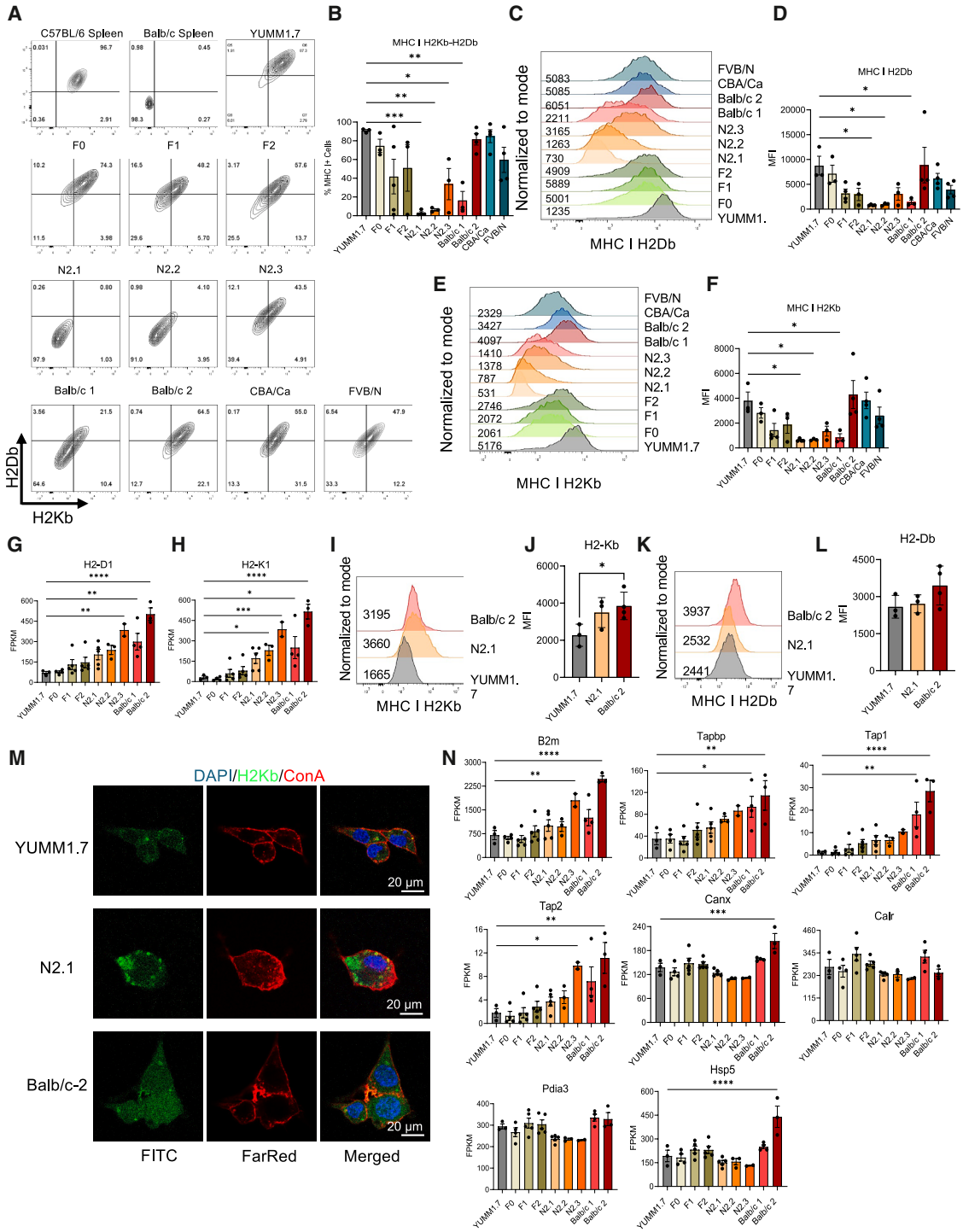

Figure 1. Expression of MHC-I during tumor passaging

(A) Surface expression levels of H2-D^b and H2-K^b by flow cytometry in YUMM1.7 cells and each tumor passage.

(B) Percentage of MHC-I$^+$ cells.

(C) Histogram plots showing the MFI distributions of H2-D^b.

(D) MFI of H2-D^b.

(E) Histogram plots showing the MFI distributions of H2-K^b.

(F) MFI of H2-K^b.

(G) RNA-seq counts (Fragments Per Kilobase of transcripts per Million mapped reads, FPKM) for *H2-D1*.

(legend continued on next page)

The proportion of takes in the F2 hybrid was higher than expected from the Mendelian segregation of MHC genes.[23] However, it has been reported that in the F2 generation, depending on the genotype of the parent, up to 100% of mouse skin grafts can survive for 2 weeks, indicating that acute rejection is delayed or reduced in F2 mice.[23] Furthermore, genotyping confirmed that the injected F2 mice contained a high proportion of the BALB/c genome (Table S1). A significantly lower proportion of tumor takes was observed at the first passage in the N2 mouse hybrid (40% takes in N2.1), which reached 47% takes in the second N2 passage and 100% in the third N2 passage, indicating full adaptation of the tumor to this mouse hybrid (Table 1). A significant tumor rejection rate (25%) was observed when the N2-adapted tumors were injected into BALB/c mice. A second passage in the BALB/c mice fully adapted the tumors (94% takes). Passaging of these Balb/c-2 tumors into MHC-mismatched CBA/Ca and FVB/N mice showed no detectable rejection, and they also grew in C57BL/6 mice (Table 1). Importantly, no tumor grew when 10^6 YUMM1.7 cells were injected directly into either the N2 or BALB/c mice (Table 1). Thus, the adapted tumors were able to escape allogeneic rejection, in contrast to the parental YUMM1.7 cells.

Tumor growth was rapid in the F0 passage, with most tumors becoming detectable by day 6 post-injection, but was slower in the F1 mouse passage, where most tumors were detected between day 8 and 10 post-injection (Figures S4A and S4B). Furthermore, in the F1 passage, half of the tumors grew to a large size (>80 mm^3), and half remained below 50 mm^3, suggesting that some tumors were constrained by immunological or other mechanisms. A similar split into fast- and slow-growing tumors was maintained in the F2 passage. N2.3 tumors grew faster than N2.1 tumors (Figure S4B). Some tumors in the N2 and BALB/c passages started to grow, then became progressively smaller and disappeared altogether, usually 14–16 days post-injection, which is consistent with acute rejection.[4] The few tumors that grew after injection of YUMM1.7 cells into N2 and BALB/c mice were also acutely rejected (Figure S4C).

Changes in MHC-I expression during tumor passaging

A well-established mechanism for tumor immune evasion is loss of heterozygosity in MHC genes or their downregulation,[24] and, indeed, in CTVT and DFT1, the surface expression of MHC-I molecules is low.[25,26] We therefore hypothesized that tumor adaptation might have resulted in the downregulation of MHC molecules to escape allogeneic recognition. To test this hypothesis, we measured MHC-I surface expression on each tumor passage and parental YUMM1.7 cells by flow cytometry using antibodies specific for the MHC-I C57BL/6 haplotype (H-2D^b H-2K^b) (Figure 1A). The specificity of these antibodies was confirmed using C57BL/6 and BALB/c splenocytes, in which no cross-reactivity was found (Figure 1A). Nearly 90% YUMM1.7 cells expressed the C57BL/6 MHC-I haplotype; about 75% tumor cells were positive for MHC-I in the F0 passage, and this value gradually decreased in the F1 and F2 passages, reaching less than 3% in the N2.1 passage. However, the percentage of MHC-I$^+$ cells started recovering in the N2.3 passage and reached levels equal to the parental YUMM1.7 cells in Balb/c-2 tumors (Figures 1A and 1B). Similar results were found by analyzing H-2D^b and H-2K^b levels of expression (mean fluorescence intensity or MFI) (Figures 1C–1F). This unexpected result indicated that MHC downregulation was essential to escape the initial strong rejection in N21 and N2.2 mice, but a different immunological pressure was exerted at later passages, leading to the selection of tumor cells re-expressing MHC-I molecules.

We examined the RNA-seq data from isolated tumor cells for expression of the *H2-D* and *H2-K* genes and found that they were upregulated in the N2 and Balb/c passages (Figures 1G and 1H). We reasoned that the lack of MHC-I surface expression despite higher gene expression could be due to its intracytoplasmic accumulation, and we measured the level of intracellular MHC-I by flow cytometry. The levels of H2-K^b were higher in N2.1 and Balb/c-2 tumors compared to YUMM1.7 cells (Figures 1I and 1J), and similar levels of H2-D^b were detectable in all tumor passages (Figures 1K and 1L). MHC-I fluorescent immunostaining showed significant intracellular signal in N2.1 and Balb/c-2 cells (Figure 1M), which is in agreement with the higher gene expression. Thus, even if H2-D^b and H2-K^b were expressed at the same or higher levels in the N2.1 tumors compared to parental YUMM1.7 cells, some defect prevented their efficient expression at the cell surface. Reduced MHC-I surface expression in the N2 passages suggested possible defects in its assembly or processing. We therefore used the RNA-seq data to survey known genes contributing to the MHC peptide loading complex (PLC), its trafficking and processing[27] (Figure 1N). In the N2 tumors, we found no evidence of silencing of *β2m* or tapasins (*Tap*) (Figure 1N), but we found downregulation of calnexin (*Canx*), calreticulin (*Calr*), and ERp57 (*Pdia3*), which are key components of the PLC,[28] and downregulation of *Hspa5* (also called *BiP*), which is required for correct protein folding in the endoplasmic reticulum (ER) upon stress[29] (Figure 1N). It seems plausible that the higher ratio of *H2-K* and *H2-D* relative to *Pdia3, Canx*, *Calr*, and *Hsp5* impaired the assembly of

(H) RNA-seq counts (FPKM) for *H2-K1*.
(I) Histogram plots showing the MFI distributions of intracellular H2-K^b.
(J) MFI of intracellular H2-K^b.
(K) Histogram plots showing the MFI distributions of intracellular H2-D^b.
(L) MFI of intracellular H2-D^b.
(M) Immunocytochemistry to detect H2D^b and concanavalin A (ConA). Scale bars, 20 μm.
(N) RNA-seq counts (FPKM) of the indicated components of MHC-I and the peptide loading complex.
In (B), (D), and (F), YUMM1.7 ($n = 3$), F0 ($n = 3$), F1 ($n = 5$), F2 ($n = 3$), N2.1 ($n = 4$), N2.2 ($n = 3$), N2.3 ($n = 3$), Balb/c-1 ($n = 3$), Balb/c-2 ($n = 4$), CBA/Ca ($n = 4$), and FVB/N ($n = 4$). In (J) and (L), YUMM1.7 and N2.1 ($n = 3$) and Balb/c-2 ($n = 4$). In (G), (H), and (N), YUMM1.7 ($n = 3$), F0 ($n = 4$), F1 ($n = 5$), F2 ($n = 5$), N2.1 ($n = 5$), N2.2 ($n = 3$), N2.3 ($n = 2$), Balb/c-1 ($n = 4$), and Balb/c-2 ($n = 3$). Statistical analysis was carried out using one-way ANOVA. Each dot represents a different tumor. Data represented as mean ± SEM, except (J) and (L) where data are represented as mean ± SD. * Denotes ($p \leq 0.05$), ** denotes ($p \leq 0.01$), *** denotes ($p = 0.001$), and **** denotes ($p < 0.0001$).

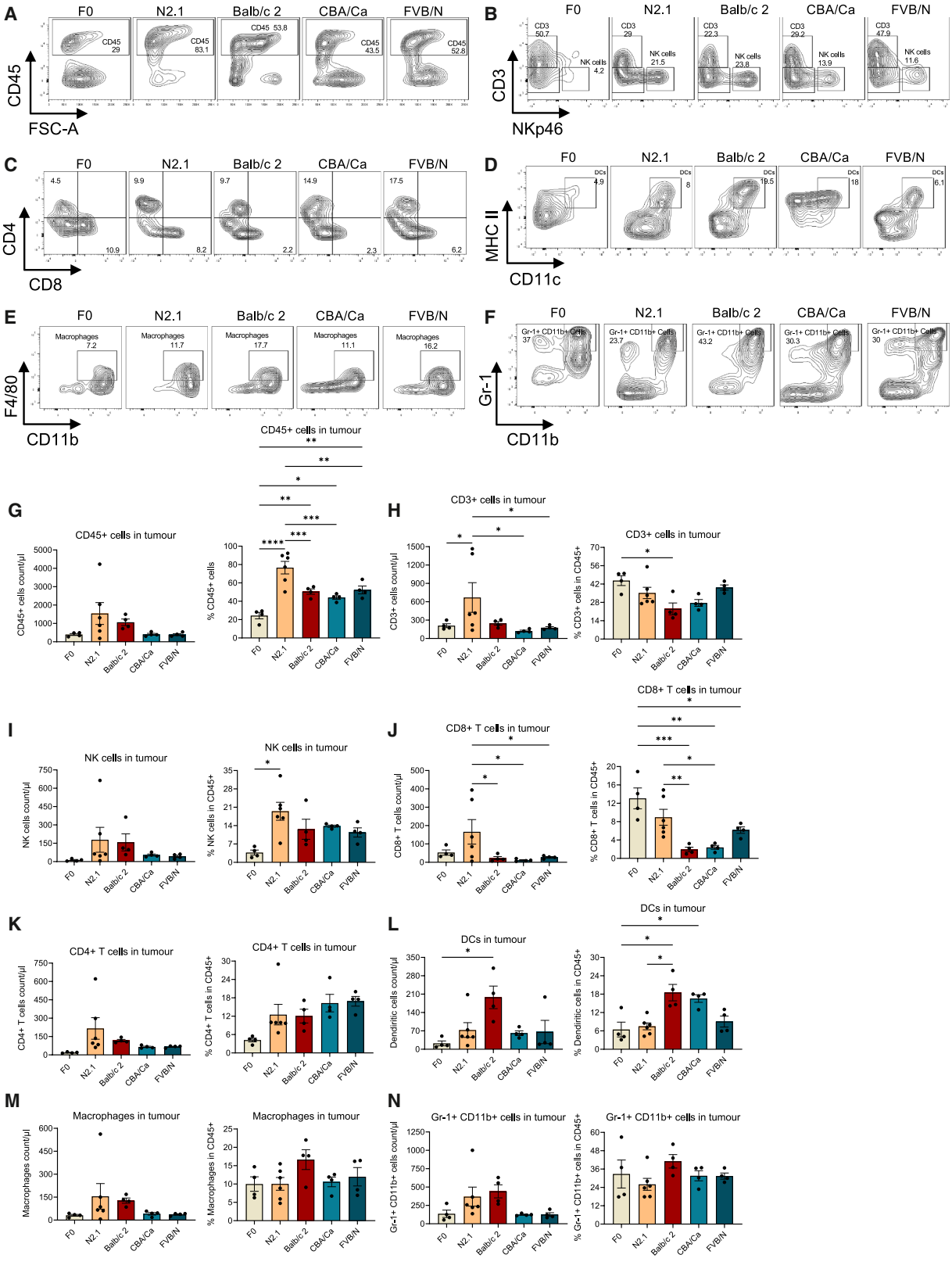

(legend on next page)

functional MHC molecules, at least in the N2 tumor cells, although other mechanisms may also be at play.

Profiling immune infiltration in the different tumor passages

To examine the tumor immune microenvironment (TIME) at each passage, freshly dissociated samples were analyzed by multiparameter flow cytometry to identify T cells ($CD45^+$ $CD3^+$ $CD4^+$ or $CD8^+$), NK cells ($CD45^+$ $CD3^-$ NKp46+), dendritic cells ($CD45^+$ $CD3^-$ MHC-II^+ $CD11c^+$), macrophages ($CD45^+$ $CD3^-$ $CD11b^+$ $F4/80^+$), and granulocytic myeloid-derived suppressor cells ($CD45^+$ $CD11b^+$ Gr-1^+).[30–33] The gating strategy is described in Figure S5. The number of $CD45^+$ leukocytes and their relative percentage were highest in N2.1 tumors, and then decreased in the Balb/c-2, CBA, and FVB/N tumors, indicating that these tumors were less immunogenic (Figures 2A and 2G; Table S2). We found more infiltrating $CD3^+$ T cells in the N2.1 tumors relative to the other passages, although their relative proportion was lower in Balb/c tumors (Figures 2B and 2H). N2.1 tumors also comprised a greater proportion of NK cells compared to the other passages (Figures 2B and 2I; Table S2).

N2.1 tumors contained more infiltrating $CD8^+$ T cells than the other passages (Figures 2C and 2J). The greater $CD8^+$ T cell infiltration in the TIME of N2.1 tumors is consistent with the high rejection rates observed in this passage and may explain the selection of cells with lower MHC-I expression, a known mechanism of cancer immune evasion.[34] There was a trend for more $CD4^+$ T cells infiltrating N2.1 than F0 tumors, which progressively reduced in later passages (Figures 2C–2K). Furthermore, the proportion of $CD4^+$ T cells expressing activation marker CD44 was lower in the N2.1, Balb/c-2, CBA, and FVB/N tumors than in F0 tumors; in N2.1 tumors, fewer cells expressed activation and residency marker CD69,[35,36] whereas PD-1, a suppressive marker that is highly expressed on dysfunctional tumor-infiltrating lymphocytes,[37] was upregulated in all the tumor passages compared to F0 (Figures S6A–S6C). Too few $CD8^+$ T cells were recovered from the late tumor passages to allow robust analyses of CD44, CD69, and PD-1.

For the myeloid compartment, there was an overall greater infiltration of dendritic cells (DCs) in all tumor passages compared to F0, with a peak found in Balb/c-2 tumors (Figures 2D and 2L). Furthermore, there was a trend for more tumor-associated macrophages (TAMs) (Figures 2E and 2M) and Gr-1^+ $CD11b^+$ cells (Figures 2F and 2N) in N2.1 and Balb/c-2 tumors compared to the other passages. The low rejection rate detected in Balb/c-2 tumors suggests that infiltrating DCs and macrophages might have had a suppressive function, as previously reported in several types of cancer, including melanoma.[38]

To assess the TIME across tumor passages, bulk RNA-seq was performed on whole F0, N2.1, Balb/c-2, and CBA tumors and deconvoluted using Murine Microenvironment Cell Population counter (mMCP) and CIBERSORT, which leverage reference signatures of mouse immune cells to estimate the composition of immune cell populations within bulk tumors.[39,40] mMCP analysis revealed a statistically significant increase in $CD8^+$ T cells and monocytes/macrophages in N2.1 tumors compared to F0 tumors, with these increases progressively moderating in Balb/c-2 and CBA tumors (Figures S6D–S6F). These results align with flow cytometry data. Similarly, CIBERSORT showed a significant increase in $CD8^+$ T cells from F0 to N2.1, which was tempered in Balb/c-2 and CBA tumors (Figures S6G and S6H). Additionally, CIBERSORT identified an increase in NK cell infiltration from F0 to N2.1 (Figure S6I). CIBERSORT provided specific signatures for M0, M1, and M2 macrophages,[41] revealing that M2 macrophages, known for their immunosuppressive roles, predominated across all passages, with the highest levels observed in F0 and Balb/c-2 tumors (Figure S6J). It is worth noting that mMCP does not reliably identify dendritic cells or $CD4^+$ T cells,[40] precluding direct comparison with flow cytometry data for these populations. Moreover, mMCP did not detect differences in NK cell infiltration across passages, in contrast to flow cytometry findings.

In summary, the combined flow cytometry and RNA-seq deconvolution results of the TIME suggest that $CD8^+$ T cells exerted a strong selective pressure on the N2.1 tumors, likely selecting for cells with low MHC-I expression, and that tumors have adopted additional strategies to control rejection, including the recruitment of M2 macrophages and a DC population with presumably suppressive functions.

Figure 2. Profile of the tumor-infiltrating cells in freshly dissociated tumors

(A) Flow cytometry plots showing the proportion of $CD45^+$.
(B) $CD3^+$ T cells and NK ($CD3^-$ $NKp46^+$) cells.
(C) $CD4^+$ and $CD8^+$ T cells.
(D) DCs (MHC-II^+ $CD11c^+$).
(E) Macrophages ($F4/80^+$ $CD11b^+$) cells.
(F) Neutrophils/MDSCs (Gr-1^+ $CD11b^+$).
(G) Left: number of $CD45^+$ cells/μL; right: the relative percentage of $CD45^+$ cells.
(H) Same as in (G) for $CD3^+$ cells.
(I) NK cells.
(J) $CD4^+$ T cells.
(K) $CD8^+$ T cells.
(L) DCs.
(M) Macrophages.
(N) Gr-$1^+$$CD11b^+$ cells.

In (G–N), F0 ($n = 4$), N2.1 ($n = 6$), Balb/c-2 ($n = 4$), CBA/Ca ($n = 4$), and FVB/N ($n = 4$). Statistical analysis was carried out using two-way ANOVA with Tukey's multiple comparison correction. Each dot represents a different tumor. Data are represented as mean ± SEM. * Denotes ($p \leq 0.05$), ** denotes ($p \leq 0.01$), *** denotes ($p = 0.001$), and **** denotes ($p < 0.0001$). See also Table S2; Figures S5 and S6.

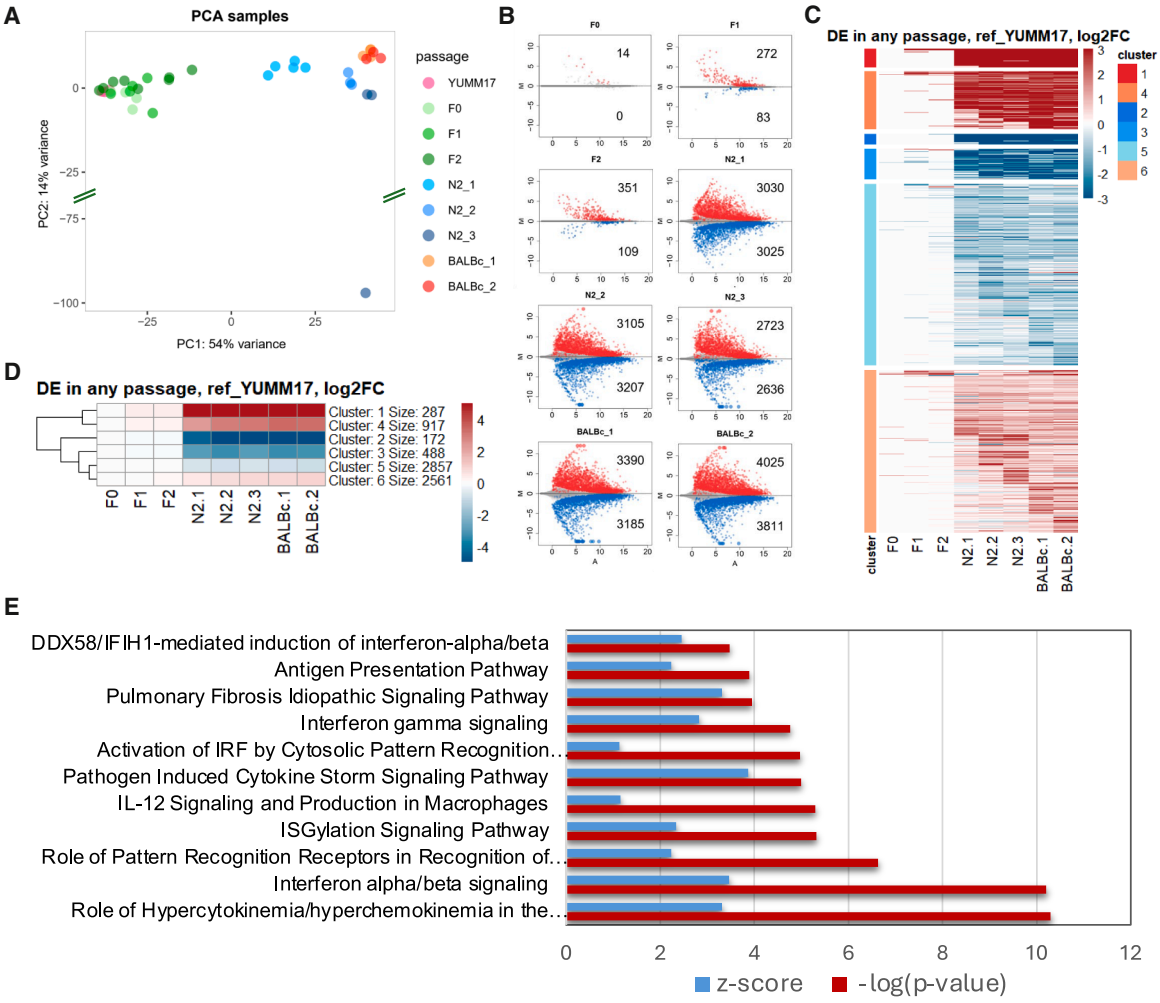

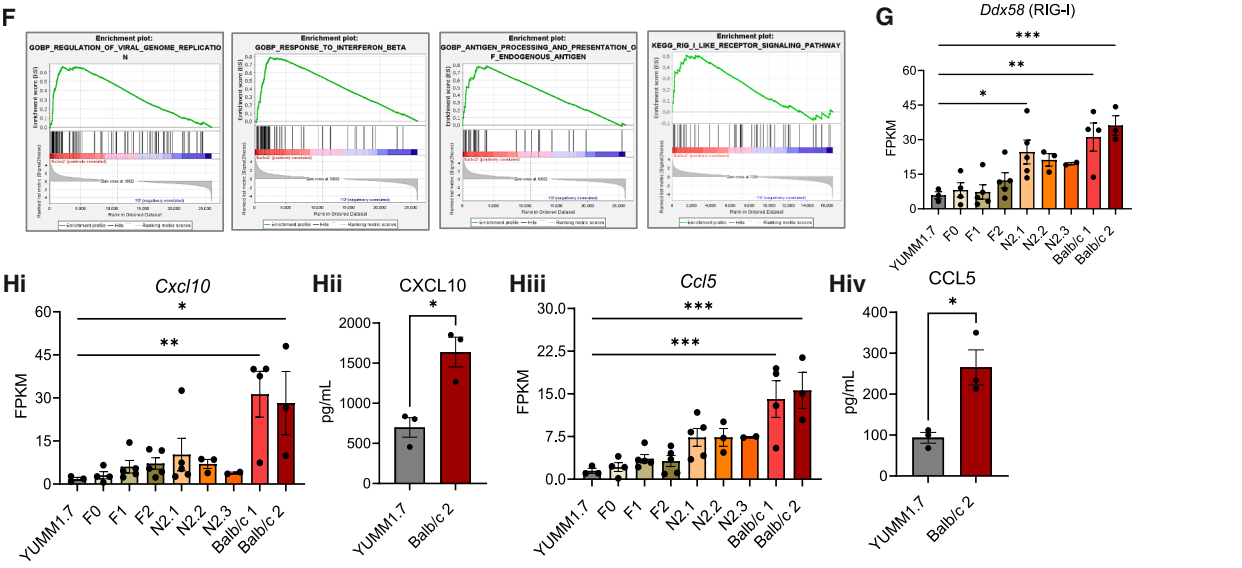

(legend on next page)

Gene expression analysis reveals an antiviral immune signature and RTEs upregulation in the tumor cells

To better understand the evolution of the tumors and the mechanisms leading to tolerance, we performed bulk RNA-seq on tumor cells to identify differentially expressed genes (DEGs) from F0 to Balb/c-2 passages, which evaded allogeneic rejection.

PolyA RNA was extracted from dissociated tumor cells after 2–4 passages *in vitro*. The number of mappable reads was uniform across samples, ranging from 3–5 $\times 10^7$ (Figure S7A). To assess potential contamination of the tumor cells with host immune cells, we determined the number of *Ptprc* reads (encoding CD45) and housekeeping ribosomal protein L5 (*rpl5)* reads, which demonstrated the lack of detectable sample contamination with $CD45^+$ leukocytes (Figure S7B). Principal component analysis (PCA) showed poor separation of YUMM1.7, F0, F1, and F2 tumors; however, N2.1, N2.2, and N2.3 tumors formed distinct clusters. Balb/c-1 and Balb/c-2 tumors grouped in one cluster that was distinct from the other clusters (Figure 3A). One N2.3 sample was an outlier, and subsequent gene expression analysis indicated that this sample was, in fact, muscle, presumably due to contamination of the biopsy. PCA suggested stepwise changes in global gene expression between the early passages (YUMM1.7 to F2), the three N2 passages, and the late passages (Balb/c). The number of DEGs relative to parental YUMM1.7 cells was low (14 upregulated and zero downregulated, at false discovery rate 5%) in F0, progressively growing in F1 (272 up and 83 down) and F2 (351 up and 109 down) tumors, and then the same step change observed by PCA was also detected in the number of DEGs, which increased rather abruptly in the N2 passages (3030 up and 3025 down) and remained high in the Balb/c passages (Figure 3B; Table S3). We performed unsupervised hierarchical clustering of the DEGs (Figure 3C) and detected three clusters of upregulated and three clusters of downregulated genes, and most changes occurred at the N2.1 passage.

Using k-means hierarchical clustering, we further identified clusters 1 and 2, which contained DEGs abruptly upregulated or downregulated, respectively; cluster 3, which contained DEGs progressively downregulated; and cluster 4, which contained DEGs progressively upregulated. Clusters 5 and 6 contained DEGs that were modestly down or upregulated, respectively (Figures 3D and S7C). We grouped clusters 1 and 4, and 2 and 3, and performed gene pathway analysis by ingenuity pathway analysis (IPA) and gene set enrichment analysis (GSEA) using the Kyoto Encyclopedia of Genes and Genomes (KEGG) and gene ontology (GO) databases. Cluster grouping allowed for more robust statistical analysis, even if it meant losing some resolution of the time of gene activation.

In clusters 2 + 3 (downregulated genes), IPA did not identify statistically significant pathways, and GSEA showed modest overlap, including DNA replication and repair and vesicle transport (Table S4). In contrast, gene clusters 1 + 4 showed significant pathway enrichment for antiviral responses, responses to IFN, antigen presentation, and pattern recognition receptor (PRR) activation, including the RNA cytosolic sensor DDX58 (RIG-I)[42] (Figure 3E). There was an excellent overlap between IPA and GSEA for the upregulated pathways, including RIG-I signaling (Figures 3F and 3G; Table S4). These results demonstrated that the tumor cells acquired an antiviral signature, which was remarkably similar to the signature detected in mouse melanoma cells selected for their ability to metastasize in lymph nodes.[43] CXCL-10 (IP-10) and CCL5 chemokines were key components of the antiviral signature; hence, we measured their expression by ELISA in tissue culture supernatants and found significantly higher values in Balb/c-2 relative to YUMM1.7 cells, which supported the GSEA results (Figure 3H). A hypermetabolic phenotype was previously reported in melanoma cells selected *in vivo* for full resistance to combined immune checkpoint blockade.[14] We therefore examined by GSEA the pathways for cellular response to oxidative stress (GO:0034599), hypoxia (GO:1900037), oxidative phosphorylation (OxPhos) (GO:0006119), and glycolytic processes (GO:0006096). Although hypoxia, OxPhos, and glycolytic processes were not in the top 300 hits, the cellular response to oxidative stress pathway (GO:0034599) was significantly enriched in cells after the N2.1 passage (NES 1.69 and $p < 0.001$) (Figure S7D). Furthermore, broad upregulation of metabolic genes was detected at the N2 and later passages (Figure S7E). Overall, the changes in the metabolic pathways were weaker than those for the antiviral response pathways.

The antiviral signature detected in the late tumor passages was unexpected and suggested an ongoing viral infection or mimicry of viral infection, which would trigger cytosolic nucleic acid sensing and activation of innate immunity. Transplantable mouse tumor cell lines often carry infectious retroviruses, derived from recombination between defective

Figure 3. The transcriptional profile of the tumor cells during passaging

(A) PCA using log-transformed counts of each tumor passage and YUMM1.7 cells.

(B) DEGs (red is upregulated and blue is downregulated) at each tumor passage relative to parental YUMM1.7 cells. *y* axis M = log2(fold change); *x* axis A = mean normalized counts.

(C) Unsupervised hierarchical clustering of DEGs in each tumor passage.

(D) k-means hierarchical clustering with k = 6 of log2(fold change) values in each tumor passage relative to YUMM1.7 cells.

(E) IPA after inputting DEGs for cluster 1 + 4.

(F) GSEA plots for Balb/c-2 cells versus YUMM1.7 cells.

(G) Expression (FPKM) of *RIG-I* in the different tumor passages.

(H) (i) Expression levels of *Cxcl10* (FPKM) in the different tumor passages. (ii) CXCL10 protein levels measured by ELISA in culture supernatants. (iii) Expression levels of *Ccl5* (FPKM) in the different tumor passages. (iv) CCL5 protein levels measured by ELISA in culture supernatants. For RNAseq in (G), (H[i]), and (H[iii]) YUMM1.7 ($n = 3$), F0 ($n = 4$), F1 ($n = 4$), F2 ($n = 5$), N2.1 ($n = 5$), N2.2 ($n = 3$), N2.3 ($n = 2$), Balb/c-1 ($n = 4$), and Balb/c-2 ($n = 3$). Statistical analysis was carried out using one-way ANOVA. For ELISA, YUMM1.7 ($n = 3$) and Balb/c 2 ($n = 3$). Statistical analysis was carried out using unpaired t test with Welch's correction. Data represented as mean ± SEM. * Denotes ($p \leq 0.05$), ** denotes ($p \leq 0.01$), *** denotes ($p = 0.001$), and **** denotes ($p < 0.0001$). See also Tables S3 and S4; Figures S7 and S8.

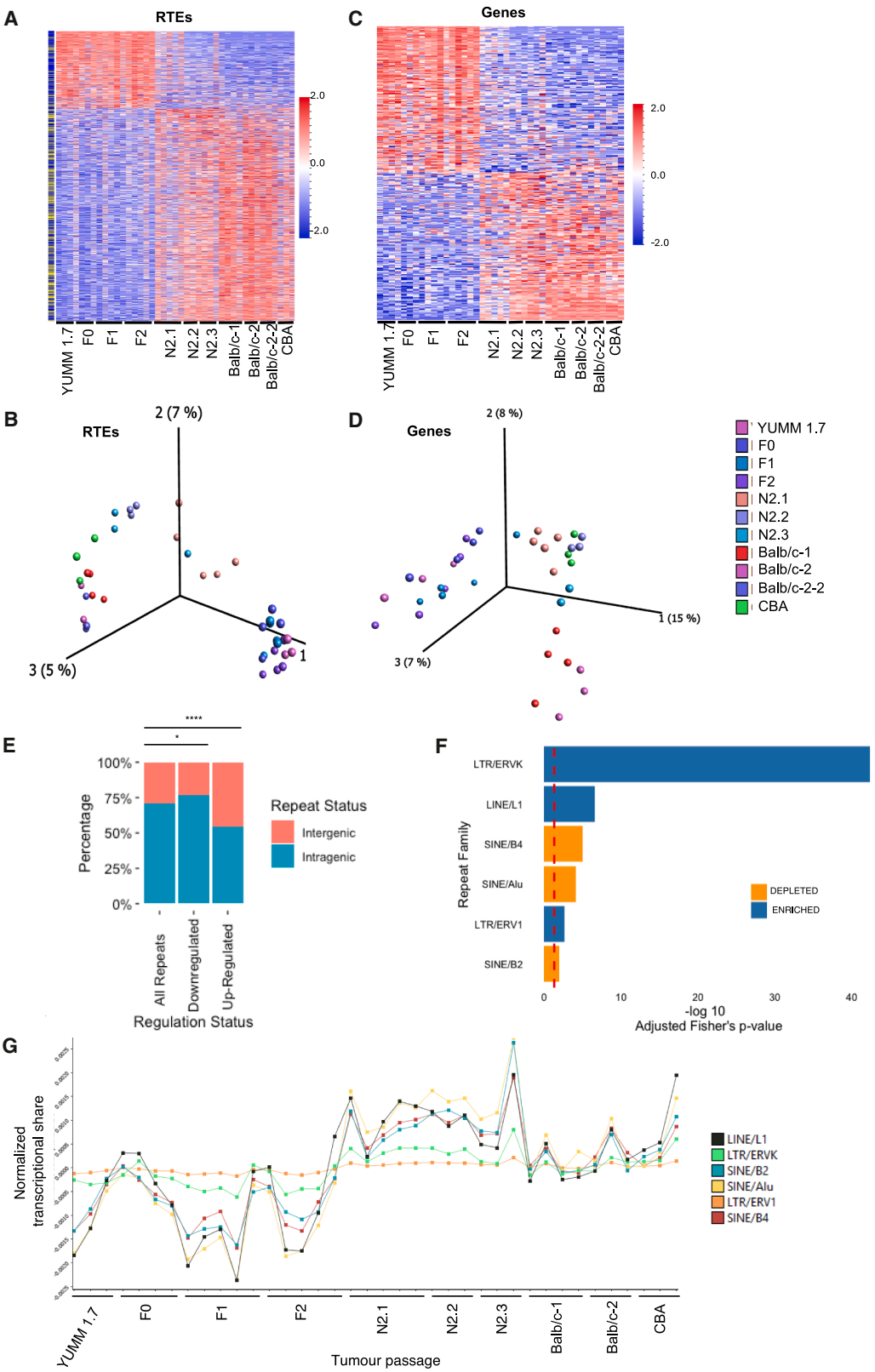

(legend on next page)

endogenous retroviruses (ERVs), which restore infectivity.[44] Typically, restoration of endogenous retrovirus (ERV) infectivity in C57BL/6 mice involves recombination with *Emv2*, a single copy endogenous murine leukemia virus (MLV) on this genetic background, which provides a functional ecotropic MLV envelope glycoprotein.[44] We therefore applied an analysis pipeline for the expression of endogenous MLVs, as well as all other retrotransposable elements (RTEs) in the mouse genome.[45] Expression of ecotropic MLV, reported by *Emv2*-related sequences, or other endogenous MLV provirus, did not appreciably change between YUMM1.7 cell passages, arguing against the presence of *Emv2*-based infectious MLVs in these cells (Figure S7F).

In contrast, this analysis identified numerous RTEs, which were significantly modulated between YUMM1.7 and Balb/c-2 cells, with a clear switch at the N2.1 passage (Figures 4A and 4B). This clear demarcation at N2.1 was also found for the DEGs (Figures 4C and 4D), indicating that tumor cells escape from allogeneic rejection correlated in time with the upregulation of RTEs and the induction of the antiviral immune signature. RTEs that were significantly upregulated in late passages included many intergenic integrations, indicating autonomous regulation (Figures 4A and 4E). Downregulated RTEs were mainly intragenic, indicating they were controlled by the gene within which they had integrated (Figures 4A and 4E). Compared with RTEs found in the whole genome, LTR/ERVK and LTR/ERV1 subfamilies of the long terminal repeat (LTR) elements, as well as LINE/L1 elements, were enriched after the N2.1 passage (Figure 4F). In contrast, expressed short interdispersed nuclear elements (SINE)/B4, SINE/Alu, and SINE/B2 subfamilies of non-LTR elements were less diverse after the N2.1 passage (Figure 4F). Notably, the overall share of transcripts was significantly increased for almost all these subfamilies at the N2.1 and later passages (Figure 4G). These results indicated strong transcriptional induction of diverse LTR and LINE elements, as well as of the highly specific SINE/Alu, SINE/B2, and SINE/B4 subfamily members. They further suggested that the acquisition of resistance to allogeneic rejection in this system was accompanied by upregulation of independently transcribed RTEs, rather than emergence of replication-competent MLVs. Given the established ability of dysregulated RTEs to activate innate immunity,[46] our findings also implicated RTEs in the activation of the IFN pathway during tumor passaging, leading to the antiviral and inflammatory signature detected in N2 and Balb/c tumors.

To probe the functional significance of the antiviral and IFN-response related signature, we examined the expression of a subset of genes known to be induced by IFN, reduce allograft rejection, and promote maternal-fetal tolerance or tumor immune evasion[47–51] (Figure S8A; Table S3). Relative to the parental YUMM1.7 cells, Balb/c-2 tumor cells showed significant upregulation of immunosuppressive molecules PD-L1, Gal-9, B7-H3 and H-2Q, H-2T, and H-2M encoding for the non-classical MHC molecule Qa-1, the homolog of human HLA-E.[52,53] For several of these genes, this trend was already detected in the N2 tumors (Figure S8B). Enhanced surface expression of PD-L1 and Qa-1 was confirmed by flow cytometry (Figures S8C and S8D). These results indicated that induction of an inflammatory signature proceeded in parallel with the upregulation of immune-protective molecules in tumor cells.

PD-L1/PD-1 interactions and non-classical MHC are critical for tumor tolerance

RTEs can be sensed by cytosolic PRRs, including RIG-I,[54] triggering an IFN response, and our gene pathway analysis showed upregulation of RIG-I signaling, pointing to a possible connection between activated RTEs, RIG-I, and the antiviral signature found in the transplantable tumor cells. A major RIG-I ligand is RNA polymerase III-transcribed Alu elements, as these lack the 5′ modifications that otherwise prevent RIG-I sensing.[55] Consistent with a role for Alu elements in inducing a RIG-I-dependent antiviral signature, we found increased transcription of SINE/Alu elements that would be sensed by RIG-I in the late tumor passages (Figure 4G), coinciding with the induction of the antiviral signature. To assess the contribution of RIG-I, we knocked it out (KO) in Balb/c-2 tumor cells by CRISPR-Cas9 using two guide RNAs (gRNAs) targeting exons 3 and 4 (Figure 5A). Four clones were selected, but the only clone with KO of both exons showed poor viability, and so we performed subsequent experiments using clone 9 (exon 3 KO) and clone 23 (exon 4 KO) (Figure 5B). Balb/c-2 tumors featured upregulation of MHC-I, PD-L1, and Qa-1 expression relative to YUMM1.7 cells, and we, therefore, tested if *RIG-I* KO affected the expression of these genes. Analysis of the two KO clones by flow cytometry detected significant

Figure 4. Analysis of RTEs expression during tumor passaging

(A) Heatmap of repeat expression per cell line measured. Repeats are filtered for a t test between tumor passages before and after N2.1 with a q value < 0.05, fold change > 2, and SD > 0.39. Heatmap made with *z*-scores. Intergenic repeats are annotated in yellow, and intragenic repeats are annotated in blue. Balb/c-2-2 is a repeat of Balb/c-2.

(B) PCA plot of repeat expression as filtered in (A).

(C) Heatmap of *z*-scores of all genes passing the statistical tests; t test between cell lines before and after N2.1 with a q value < 0.05, fold change > 2, and SD > 0.39.

(D) PCA of samples using the gene list in (B).

(E) Scaled barplot of the ratios of intergenic and intragenic repeats across the whole genome (all repeats), and those which are upregulated or downregulated as in (A). * Adjusted Fisher's exact p = 1.61e-02 and adjusted chi-squared p = 1.79e-02; **** adjusted Fisher's exact p = 1.67e-39 and adjusted chi-squared p = 1.05e-42.

(F) Barplot of the −log10 adjusted Fisher's test p value for the enrichment of each repeat superfamily in upregulated or downregulated repeats as defined by Fisher's exact test in (A). A red dotted line is used to show p = 0.05. A Fisher's odds ratio > 1 indicates enrichment in passages from N2.1 onwards compared to the whole genome.

(G) Normalized expression of the indicated subfamilies of RTE at distinct tumor passages. Only RTE subfamilies with significant enrichment and expression changes between tumor passages before and after N2.1 are shown.

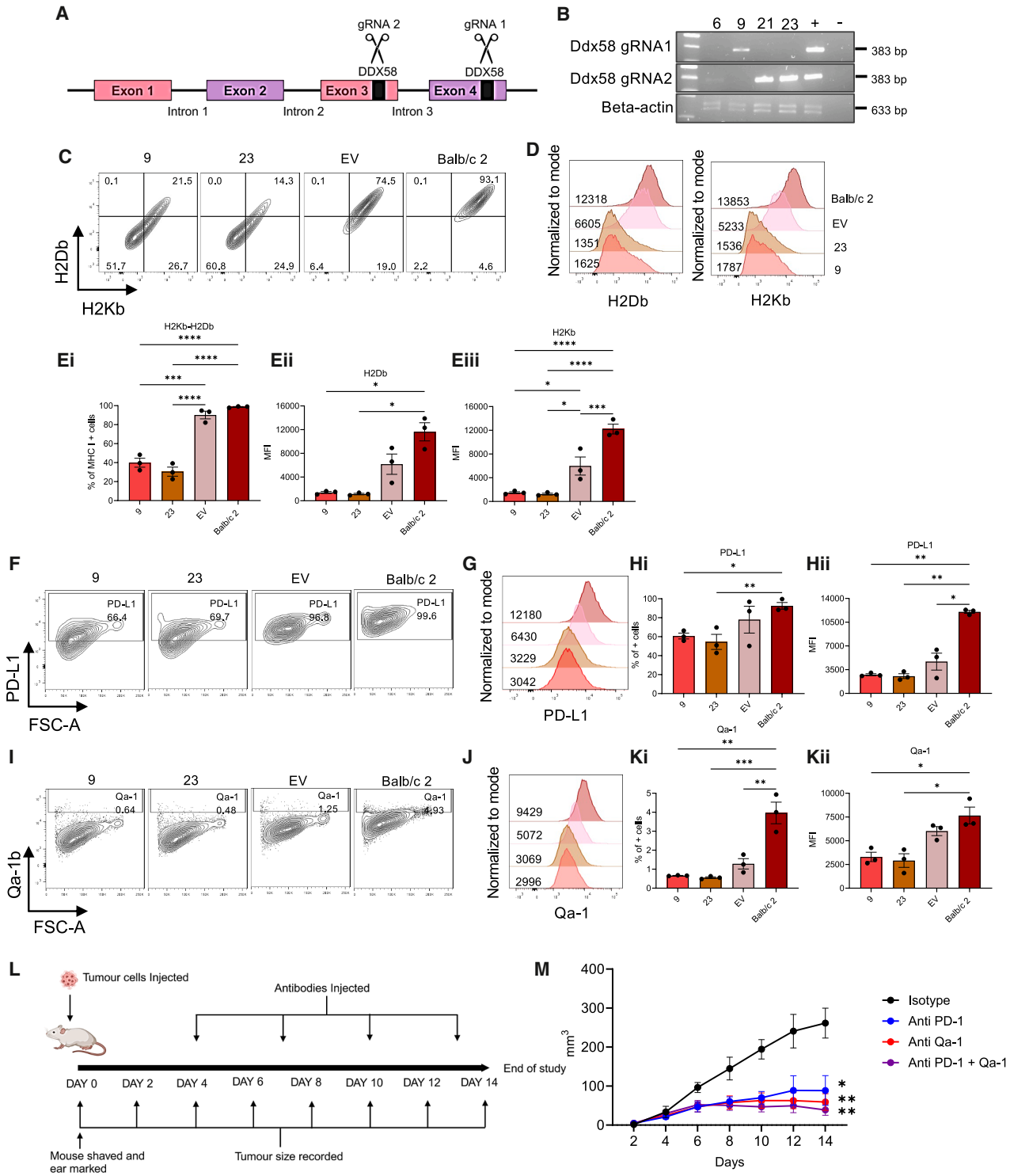

Figure 5. RIG-I, PD-L1, and Qa-1 regulate tumors' escape from allogeneic rejection

(A) Schematic depiction of the *Ddx58* (RIG-I) exons targeted by the gRNAs in the CRISPR-Cas9 lentiviral vector.

(B) Gel electrophoresis of PCR products specific for *Ddx58* exon 1 or 2 after amplification of DNA from four clones.

(C) Surface expression levels of H2Db and H2Kb by flow cytometry in clones 9 and 23, empty vector (EV), and parental Balb/c-2 cells.

(D and E) (D) Histogram plots showing the MFI distributions of H2Db and H2Kb; (E) left: percentage of $H2Db^{+}$ $H2Kb^{+}$ cells in clones 9 and 23, EV, and Balb/c-2 cells; middle and right panels: MFI of H2Db and H2Kb, respectively.

(legend continued on next page)

downregulation of H-2K^b and H-2D^b surface expression (Figures 5C–5E). In a similar fashion, we detected lower surface expression of PD-L1 (Figures 5F–5H) and Qa-1 (Figures 5I–5K) in *RIG-I* KO cells compared to the parental Balb/c-2 cells. Notably, the control empty puromycin resistance-expressing vector (EV) also reduced somewhat the MHC-I and PD-L1 MFI values and the percentage of Qa-1$^+$ cells, albeit not to the same extent as the KO cells, suggesting that selection with puromycin or insertion of the retroviral construct might affect expression of these molecules.

To test if *RIG-I* KO was sufficient to trigger rejection of Balb/c-2 tumor cells, we injected BALB/c mice with KO clone 9, clone 23, or EV cells. We detected three takes with KO clone 9, no takes with KO clone 23, and one take with EV cells. In contrast, there was a 100% take rate in BALB/c mice injected with the parental Balb/c-2 cells (Table S5). The rejection of *RIG-I* KO cells and EV control cells was likely due to the reduced level of expression of PD-L1 and Qa-1. To further test the hypothesis that PD-L1 and Qa-1 were critical to protect the tumor from rejection, we injected BALB/c mice with Balb/c-2 tumor cells, and when tumors became palpable, mice were administered intraperitoneally every 3 days with anti-PD-1 antibodies, anti-Qa-1 antibodies, the two antibodies combined, or isotype control antibodies. Treated mice were monitored for 14 days, and tumor growth was measured regularly (Figure 5L). Treatment with either anti-PD1 or anti-Qa1 antibodies significantly reduced tumor growth relative to isotype antibodies, and treatment with a combination of anti-PD1 and anti-Qa1 antibodies induced tumor regression (Figure 5M; Table S6). These results confirmed that high expression levels of PD-L1 and Qa-1 were required for allotransplantation tolerance, although other molecules not tested here might also have contributed.

The antiviral signature found in Balb/c-2 cells was reminiscent of a similar profile detected in a subset of human melanomas that did not respond to first-line treatment with anti-CTLA4 antibodies (ipilimumab) but responded to second-line PD-L1/PD-1 signaling blockage by anti-PD-1 antibodies.[56] Similarly to Balb/c-2 tumor cells, GSEA in ipilimumab-experienced melanomas that responded to anti-PD-1 treatment showed enrichment for "allograft rejection," "IFNγ," "IFN response," "inflammatory response" pathways, and upregulated MHC-I and MHC-II genes.[56] Notably, despite the inflammatory signature and MHC-I upregulation, these melanomas were able to grow and metastasize but became susceptible to anti-PD-1 treatment. Because of these transcriptional and phenotypic similarities, we investigated whether the core Balb/c-2 signature, defined by clusters 1 and 2 (Figure 3D), could also be detected in the human melanomas and if this signature increased their susceptibility to anti-PD-1 treatment. Not only were we able to detect the Balb/c-2 signature, but we also found that human melanomas with the Balb/c-2 tumor signature were associated with significantly better overall survival odds after anti-PD-1 treatment than melanomas lacking the signature (Figure 6A), even after correcting for sex and ipilimumab treatment (Figure S9). Furthermore, the patients treated with ipilimumab and with the Balb/c-2 signature also displayed markedly improved progression-free survival after PD-1 blockade (Figure 6B). Therefore, the Balb/c-2 tumor antiviral signature was associated with greater sensitivity to PD-L1/PD-1 blockage. In this respect, the phenotype observed in patients and the one observed with Balb/c-2 tumors was similar, reinforcing the notion that the antiviral immune signature did allow tumor growth, and perhaps even facilitated it by promoting immune evasion and accumulation of neoantigens, but at the same time, it made tumors more dependent on PD-L1 signaling for immunological escape.

DISCUSSION

Guided by tumor passaging experiments conducted in the 1920s, we obtained a melanoma that escaped allogeneic rejection in multiple mismatched mouse strains. A key feature associated with tumor immune escape was the acquisition of an antiviral immune signature and simultaneous activation of intergenic RTEs and the RIG-I nucleic acid-sensing pathway. This occurred rather abruptly at the N2 passage, which showed significant rejection of transplanted tumors, supporting a causal link, whereby tumor cells that evolved those specific features survived immune attack and expanded. Those tumor cell features were maintained in subsequent passages, further supporting their critical role.

In our experimental model, the induction of an antiviral signature facilitated tumor immune evasion, and yet sensing of dysregulated RTEs was previously found to enhance tumor immunogenicity.[46] Treatment of colorectal carcinoma and melanoma cells with a combination of DNA demethylating agents and inhibitors of histone acetyltransferase was shown to reduce tumor cell growth *in vitro* and to make tumors more susceptible to immune checkpoint therapy. This effect was mediated by the transcriptional upregulation of RTEs, their sensing, and the induction of an antiviral state.[57–59] Furthermore, loss of epigenetic regulators controlling RTEs' expression can hinder tumor growth in mice,[60,61] although this is not always seen in humans.[62]

(F) Surface expression levels of PD-L1 by flow cytometry in clones 9 and 23, EV, and parental Balb/c-2 cells.
(G) Histogram plots showing the MFI distributions of PD-L1.
(H) Percentage of PD-L1$^+$ cells in clones 9 and 23, EV, and Balb/c-2 (Hi, left) and MFI values (Hii, right).
(I) Surface expression levels of Qa-1 by flow cytometry in clones 9 and 23, EV, and parental Balb/c-2 cells.
(J) Histogram plots showing the MFI distributions of Qa-1.
(K) Percentage of Qa-1$^+$ cells in clones 9 and 23, EV, and Balb/c-2 (Ki, left) and MFI values (Kii, right).
(L) Schematic depiction of the experimental set-up for the treatment of mice with anti-PD-1 and Qa-1 antibodies. 1×10^6 Balb/c-2 cells were injected into the mice, and at day 4, when tumors became palpable, mice were injected intraperitoneally with the antibodies.
(M) Tumor growth curves during treatment with the antibodies, isotype, anti-PD-1, anti-Qa-1, anti-PD-1 + Qa-1 ($n = 6$).
In (E), (H), and (K), clones 9 and 23, EV, and Balb/c-2 ($n = 3$). Statistical analysis was performed using two-way ANOVA with Tukey's correction. Each dot represents a different tumor. Data represented as mean ± SEM. * Denotes ($p \leq 0.05$), ** denotes ($p \leq 0.01$), *** denotes ($p = 0.001$), and **** denotes ($p < 0.0001$). See also Tables S5 and S6.

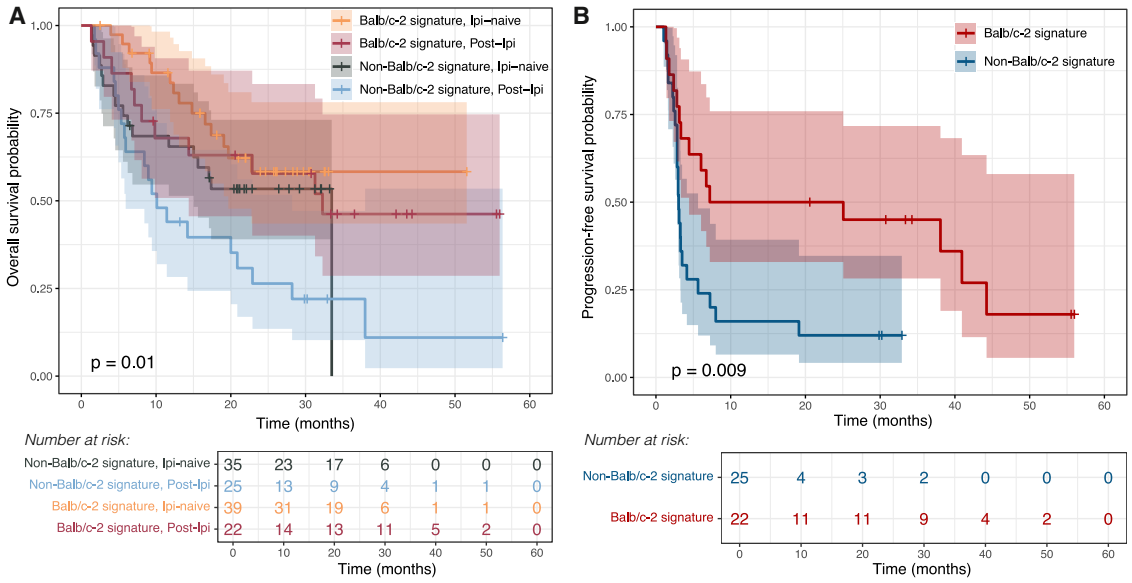

Figure 6. Human melanomas sharing the antiviral signature of Balb/c-2 cells show better response to anti-PD-1 antibodies

(A) Overall survival after anti-PD-1 treatment for patients who were either previously treated with ipilimumab (post-Ipi) or not (ipi-naïve), stratified by the presence of the Balb/c-2 signature in their tumors.

(B) Progression-free survival after anti-PD-1 treatment for patients previously treated with ipilimumab (post-ipi), stratified by the presence of the Balb/c-2 signature in their tumors. The tables under the Kaplan-Meier curves denote the numbers at risk at selected time points. See also Figure S9.

These apparently contrasting observations can be explained by the strong selective pressure applied to the tumors in our model of allotransplantation, in which only cells with highly effective compensatory mechanisms could survive. One compensatory mechanism was the upregulation of PD-L1 and Qa-1. PD-L1, by binding to PD-1 on T cells, inhibits their activation, proliferation, and survival, and its upregulation is associated with worse prognosis in patients with cancer.[63] Qa-1 and HLA-E in humans present a limited array of peptides derived from the leader sequence of classical MHC molecules. The Qa-1-peptide complex binds to the inhibitory receptor NKG2A/CD94 expressed on NK cells and subsets of $CD8^+$ T cells, effectively blocking their activation.[52,53] We postulate that further inhibition of NK cells was achieved by the upregulation of MHC-I molecules on the Balb/c-2 tumor cells. Both PD-L1 and Qa-1/HLA-E are upregulated by IFN,[64,65] and their overexpression was critical to maintain tolerance because their antibody-mediated blockage triggered tumor regression. This suggests that the antiviral response, paradoxically, by inducing surface expression of immunomodulatory molecules, may also protect against attack by infiltrating immune cells, and we speculate that, in the context of a response to infection, this mechanism may be important to limit immune-mediated damage to bystander cells that are not infected by a virus. In support of this idea, Qa-1/HLA-E were shown to protect tissues from excessive $CD8^+$ T cell activation during virus infection[53]

Remarkably, an antiviral signature similar to the one we have found in the transplantable tumors was described in mouse melanoma cells selected by serial passaging *in vivo* for high lymph node metastatic potential,[43] indicating a common evolutionary mechanism for immune evasion. Furthermore, this antiviral profile was also detected in human melanoma, including metastatic melanoma,[56] suggesting that this signature is not always sufficient *per se* to limit tumor growth or spread *in vivo*. Nonetheless, our transplantable tumor was highly sensitive to antibody-mediated blockage of PD-L1 and Qa-1, pointing to the dependence of the tumor on these immunosuppressive molecules to grow in mismatched hosts. Thus, while a strong selective pressure caused the survival and expansion of cells expressing high levels of immune-protective molecules, these same cells also became highly dependent on these molecules for their survival in a hostile environment. Our transplantable tumor, therefore, seems to exist in a "metastable" state, similarly to CTVT, in which treatment with vincristine triggers a strong pro-inflammatory immune signature, leading to tumor rejection.[15]

Another protective mechanism evolved by our transplantable tumor appeared to be the ability to attract significant amounts of M2 macrophages and DCs in the TIME. M2 TAMs are known to suppress effector immune cells by the production of soluble factors such as arginase-1 and interleukin-10, leading to tumor survival and tolerance.[66] DCs are well known to contribute to anti-tumour immunity and allograft rejection, but there is also evidence for an inhibitory or tolerogenic role of immature and certain subsets of plasmacytoid DCs, which increase allograft survival.[67,68] In agreement with earlier studies, we propose that a chronic inflammatory TIME promotes recruitment of immune suppressive myeloid cells and facilitates T cell exhaustion.[38] Thus, the chronic pro-inflammatory response induced by dysregulated RTEs appears to contribute to the adaptive immune resistance that has also been observed in human tumors.[69]

The transplantable tumor cells initially downregulated MHC-I molecules but unexpectedly re-expressed them at later stages

of passaging. Loss of MHC-I expression is a hallmark of invasive tumors,[70] and so our results are surprising but have been previously described in mouse melanomas selected *in vivo* to resist immune checkpoint therapy[14] and in some human melanomas.[56] One possibility that needs further testing is that the MHC-I was defective; however, anti-PD-1 antibodies inhibited the growth of the transplanted tumor, suggesting that MHC-I on the cell surface was functional and able to present tumour-derived antigenic peptides. We therefore favor the hypothesis that MHC-I re-expression was selected for to prevent NK-mediated cell killing at a stage when the tumor had already evolved effective mechanisms to limit cytotoxic T cell activity.

CTVT was reported to express low levels of MHC-I, sufficient to limit NK cell recognition but presumably too low to trigger cytotoxic T cell killing,[71] and this seems different from our transplantable melanoma, suggesting divergent evolutionary pathways. It should be noted, however, that CTVT has a much longer evolutionary history than our adapted tumor, and that CTVT can escape delayed rejection, which we could not test in our model. Hence, our model may represent an early adaptation stage. Notably, DFT2 has maintained MHC-I expression,[72] pointing to a shared evolutionary path in tumors that only recently became transmissible/transplantable. Similar to the transplantable melanoma, choriocarcinoma also expresses HLA-I[73] and high levels of PD-L1[74] and non-classical HLAs,[75] including after IFN treatment,[76] and is susceptible to PD-L1 antagonism.[77]

Our results revealed that the combination of an antiviral cellular state, upregulation of PD-L1, MHC-I, and HLA-E is associated with extreme forms of cancer immune evasion. In addition, heightened metabolism may also contribute to the immune evasive phenotype, as previously described.[14] Thus, the transplantation model described here should be relevant to understanding the general mechanisms of allogeneic rejection and cancer resistance to immune attack, a notion supported by the fact that HLA-E upregulation is detected in many human cancers and that blocking the HLA-E/NKG2A interaction has shown encouraging clinical responses.[53,78,79] Notably, our results also demonstrated that escape from allogeneic rejection may not be limited to the known clonally transmissible tumors.

Limitations of the study

Our study has several limitations. We have not identified the genetic and epigenetic mechanisms underpinning the pro-inflammatory signature or RTEs' upregulation. The functional link between RTEs and the inflammatory signal has been inferred based on the upregulation of SINE/Alu elements and the results in the RIG-I KO cells, but we have not pinpointed the specific RTEs involved. Lastly, we have only examined acute rejection in one experimental model.

RESOURCE AVAILABILITY

Lead contact

Requests for further information and resources should be directed to and will be fulfilled by the lead contact, Ariberto Fassati (a.fassati@ucl.ac.uk).

Materials availability

Cell lines described in this article will be made available upon request, but we require completing a material transfer agreement.

Data and code availability

- Data: raw and processed RNA-seq data for mouse tumors have been deposited in the NCBI Gene Expression Omnibus at GEO: GSE288825 (biopsies) and GSE288897 (cells) and are publicly available. Raw RNA-seq data for the human melanoma samples have been previously deposited by Li et al. (https://doi.org/10.1038/s41591-019-0654-5) at dbGaP (accession number phs000452.v3.p1) and are publicly available at https://www.ncbi.nlm.nih.gov/projects/gap/cgi-bin/study.cgi?study_id=phs000452.v3.p1. The accession numbers are also listed in the key resources table.
- Code: all custom scripts and analysis pipelines used in this study have been deposited on GitHub and are publicly available at: https://github.com/secrierlab/Metastatic-melanoma-anti-PD1/. The link is also listed in the key resources table.
- Other: any additional information required to reanalyze the data reported in this paper is available from the lead contact upon request.

ACKNOWLEDGMENTS

We thank Ben Seddon, Benny Chain, Steve Goff, Liz Murchison, Liz Simpson, Mala Maini, and Robin Weiss for advice. A.R. was supported by a PhD scholarship at UCL funded by the Ministry of Education of Saudi Arabia and by Prince Sattam bin Abdulaziz University (project no. PSAU/2025/R/1446); M.O.D. was funded by the UCL Therapeutic Acceleration Support (588091); S.N. was supported by a PhD scholarship at UCL funded by the Ministry of Education of Saudi Arabia and King Abdulaziz University; and M.S. was supported by a UKRI Future Leaders Fellowship (MR/T042184/1). This work was also funded by the Medical Research Council (MRC) grant MR/W001241/1 to A.F. and J.I.d.l.H.; and the Francis Crick Institute (CC2088 to G.K.), which receives its core funding from Cancer Research UK, the UK Medical Research Council, and the Wellcome Trust. This project has received funding from the European Research Council (ERC) to G.K. under the European Union's Horizon 2020 research and innovation program (101018670).

AUTHOR CONTRIBUTIONS

Study design and conceptualization: A.F. and A.R.; methodology: A.R., M.O.D., C.L.B., J.I.d.l.H., C.H., M.S., and G.K.; investigation and experimentation: A.R. and C.B.; formal analysis: A.R., M.O.D., J.I.d.l.H., C.H., S.N., M.S., G.K., and A.F.; data curation: A.R., J.I.d.l.H., G.K., C.H., and M.S.; writing – original draft: A.F.; writing – review and editing: A.R., M.O.D., M.S., G.K., C.H., and A.F.; supervision: A.F. and G.K.

DECLARATION OF INTERESTS

G.K. is a scientific cofounder of EnaraBio and a member of its scientific advisory board. G.K. has consulted for EnaraBio, Repertoire Immune Medicines, ErVimmune, and AdBio Partners.

DECLARATION OF GENERATIVE AI AND AI-ASSISTED TECHNOLOGIES IN THE WRITING PROCESS

During the preparation of this work, the authors used ChatGPT-4 in order to shorten the text of the eTOC summary. After using this tool or service, the authors reviewed and edited the content as needed and take full responsibility for the content of the publication.

STAR★METHODS

Detailed methods are provided in the online version of this paper and include the following:

- KEY RESOURCES TABLE

SUPPLEMENTAL INFORMATION

Supplemental information can be found online at https://doi.org/10.1016/j.celrep.2025.116288.

Received: April 24, 2025
Revised: July 23, 2025
Accepted: August 22, 2025

REFERENCES

1. Little, C.C., and Tyzzer, E.E. (1916). Further experimental studies on the inheritance of susceptibility to a Transplantable tumor, Carcinoma (J. W. A.) of the Japanese waltzing Mouse. J. Med. Res. *33*, 393–453.
2. Snell, G.D., and Jackson, R.B. (1953). The Genetics of Transplantation 1, 2. J. Natl. Cancer Inst. *14*, 691.
3. The Nobel Lectures in Immunology (1992). The Nobel Prize for Physiology or Medicine, 1980 awarded to Baruj Benacerraf, Jean Daussett & George D. Snell. Scand. J. Immunol. *35*, 373–398.
4. Moreau, A., Varey, E., Anegon, I., and Cuturi, M.C. (2013). Effector mechanisms of rejection. Cold Spring Harb. Perspect. Med. *3*, a015461. https://doi.org/10.1101/cshperspect.a015461.
5. Lakkis, F.G., and Lechler, R.I. (2013). Origin and biology of the allogeneic response. Cold Spring Harb. Perspect. Med. *3*, a014993. https://doi.org/10.1101/cshperspect.a014993.
6. Ostrander, E.A., Davis, B.W., and Ostrander, G.K. (2016). Transmissible Tumors: Breaking the Cancer Paradigm. Trends Genet. *32*, 1–15. https://doi.org/10.1016/j.tig.2015.10.001.
7. Scanlon, E.F., Hawkins, R.A., Fox, W.W., and Smith, W.S. (1965). Fatal Homotransplanted Melanoma: A Case Report. Cancer *18*, 782–789.
8. Gartner, H.V., Seidl, C., Luckenbach, C., Schumm, G., Seifried, E., Ritter, H., and Bultmann, B. (1996). Genetic analysis of a sarcoma accidentally transplanted from a patient to a surgeon. N. Engl. J. Med. *335*, 1494–1496. https://doi.org/10.1056/NEJM199611143352004.
9. Wang, X., Fu, S., Freedman, R.S., Liu, J., and Kavanagh, J.J. (2006). Immunobiology of gestational trophoblastic diseases. Int. J. Gynecol. Cancer *16*, 1500–1515. https://doi.org/10.1111/j.1525-1438.2006.00539.x.
10. Chong, A.S., Alegre, M.-L., Miller, M.L., and Fairchild, R.L. (2013). Lessons and limits of mouse models. Cold Spring Harb. Perspect. Med. *3*, a015495.
11. Strong, L.C. (1926). On the Occurrence of Mutations within Transplantable Neoplasms. Genetics *11*, 294–303.
12. Strong, L.C. (1926). Changes in the Reaction Potential of a Transplantable Tumor. J. Exp. Med. *43*, 713–724.
13. Barrett, M.K., and Deringer, M.K. (1952). Induced adaptation in a tumor: permanence of the change. J. Natl. Cancer Inst. *12*, 1011–1017.
14. Jaiswal, A.R., Liu, A.J., Pudakalakatti, S., Dutta, P., Jayaprakash, P., Bartkowiak, T., Ager, C.R., Wang, Z.Q., Reuben, A., Cooper, Z.A., et al. (2020). Melanoma Evolves Complete Immunotherapy Resistance through the Acquisition of a Hypermetabolic Phenotype. Cancer Immunol. Res. *8*, 1365–1380. https://doi.org/10.1158/2326-6066.CIR-19-0005.
15. Frampton, D., Schwenzer, H., Marino, G., Butcher, L.M., Pollara, G., Kriston-Vizi, J., Venturini, C., Austin, R., de Castro, K.F., Ketteler, R., et al. (2018). Molecular Signatures of Regression of the Canine Transmissible Venereal Tumor. Cancer Cell *33*, 620–633.e6. https://doi.org/10.1016/j.ccell.2018.03.003.
16. Murchison, E.P., Wedge, D.C., Alexandrov, L.B., Fu, B., Martincorena, I., Ning, Z., Tubio, J.M.C., Werner, E.I., Allen, J., De Nardi, A.B., et al. (2014). Transmissible [corrected] dog cancer genome reveals the origin and history of an ancient cell lineage. Science *343*, 437–440. https://doi.org/10.1126/science.1247167.
17. Meeth, K., Wang, J.X., Micevic, G., Damsky, W., and Bosenberg, M.W. (2016). The YUMM lines: a series of congenic mouse melanoma cell lines with defined genetic alterations. Pigment Cell Melanoma Res. *29*, 590–597. https://doi.org/10.1111/pcmr.12498.
18. Wang, J., Perry, C.J., Meeth, K., Thakral, D., Damsky, W., Micevic, G., Kaech, S., Blenman, K., and Bosenberg, M. (2017). UV-induced somatic mutations elicit a functional T cell response in the YUMMER1.7 mouse melanoma model. Pigment Cell Melanoma Res. *30*, 428–435. https://doi.org/10.1111/pcmr.12591.
19. Erkes, D.A., Cai, W., Sanchez, I.M., Purwin, T.J., Rogers, C., Field, C.O., Berger, A.C., Hartsough, E.J., Rodeck, U., Alnemri, E.S., and Aplin, A.E. (2020). Mutant BRAF and MEK Inhibitors Regulate the Tumor Immune Microenvironment via Pyroptosis. Cancer Discov. *10*, 254–269. https://doi.org/10.1158/2159-8290.CD-19-0672.
20. Castellani, G., Buccarelli, M., Arasi, M.B., Rossi, S., Pisanu, M.E., Bellenghi, M., Lintas, C., and Tabolacci, C. (2023). BRAF Mutations in Melanoma: Biological Aspects, Therapeutic Implications, and Circulating Biomarkers. Cancers (Basel) *15*, 4026. https://doi.org/10.3390/cancers15164026.
21. Lefranc, M.P., Giudicelli, V., Kaas, Q., Duprat, E., Jabado-Michaloud, J., Scaviner, D., Ginestoux, C., Clément, O., Chaume, D., and Lefranc, G. (2005). IMGT, the international ImMunoGeneTics information system. Nucleic Acids Res. *33*, D593–D597. https://doi.org/10.1093/nar/gki065.
22. Little, C.C., and Johnson, B.W. (1922). The inheritance of susceptibility to implants of splenic tissue in mice. 1. Japanese waltzing mice, albinos, and their F1 generation hybrids. Exp. Biol. Med. (Maywood). *19*, 163–167.
23. Barnes, A.D., and Krohn, P.L. (1957). The estimation of the number of histocompatibility genes controlling the successful transplantation of normal skin in mice. Proc. R. Soc. Lond. B Biol. Sci. *146*, 505–526. https://doi.org/10.1098/rspb.1957.0027.
24. Garrido, F., Ruiz-Cabello, F., and Aptsiauri, N. (2017). Rejection versus escape: the tumor MHC dilemma. Cancer Immunol. Immunother. *66*, 259–271. https://doi.org/10.1007/s00262-016-1947-x.
25. Cohen, D. (1985). The canine transmissible venereal tumor: a unique result of tumor progression. Adv. Cancer Res. *43*, 75–112.
26. Siddle, H.V., Kreiss, A., Tovar, C., Yuen, C.K., Cheng, Y., Belov, K., Swift, K., Pearse, A.M., Hamede, R., Jones, M.E., et al. (2013). Reversible

epigenetic down-regulation of MHC molecules by devil facial tumour disease illustrates immune escape by a contagious cancer. Proc. Natl. Acad. Sci. USA *110*, 5103–5108. https://doi.org/10.1073/pnas.1219920110.

27. Olson, E., and Raghavan, M. (2023). Major histocompatibility complex class I assembly within endolysosomal pathways. Curr. Opin. Immunol. *84*, 102356. https://doi.org/10.1016/j.coi.2023.102356.
28. Diedrich, G., Bangia, N., Pan, M., and Cresswell, P. (2001). A role for calnexin in the assembly of the MHC class I loading complex in the endoplasmic reticulum. J. Immunol. *166*, 1703–1709. https://doi.org/10.4049/jimmunol.166.3.1703.
29. Braakman, I., and Bulleid, N.J. (2011). Protein folding and modification in the mammalian endoplasmic reticulum. Annu. Rev. Biochem. *80*, 71–99. https://doi.org/10.1146/annurev-biochem-062209-093836.
30. Bronte, V., Brandau, S., Chen, S.H., Colombo, M.P., Frey, A.B., Greten, T. F., Mandruzzato, S., Murray, P.J., Ochoa, A., Ostrand-Rosenberg, S., et al. (2016). Recommendations for myeloid-derived suppressor cell nomenclature and characterization standards. Nat. Commun. *7*, 12150. https://doi.org/10.1038/ncomms12150.
31. Dean, I., Lee, C.Y.C., Tuong, Z.K., Li, Z., Tibbitt, C.A., Willis, C., Gaspal, F., Kennedy, B.C., Matei-Rascu, V., Fiancette, R., et al. (2024). Rapid functional impairment of natural killer cells following tumor entry limits anti-tumor immunity. Nat. Commun. *15*, 683. https://doi.org/10.1038/s41467-024-44789-z.
32. Diao, J., Gu, H., Tang, M., Zhao, J., and Cattral, M.S. (2018). Tumor Dendritic Cells (DCs) Derived from Precursors of Conventional DCs Are Dispensable for Intratumor CTL Responses. J. Immunol. *201*, 1306–1314. https://doi.org/10.4049/jimmunol.1701514.
33. Qiao, T., Yang, W., He, X., Song, P., Chen, X., Liu, R., Xiao, J., Yang, X., Li, M., Gao, Y., et al. (2023). Dynamic differentiation of F4/80+ tumor-associated macrophage and its role in tumor vascularization in a syngeneic mouse model of colorectal liver metastasis. Cell Death Dis. *14*, 117. https://doi.org/10.1038/s41419-023-05626-1.
34. Dhatchinamoorthy, K., Colbert, J.D., and Rock, K.L. (2021). Cancer immune evasion through loss of MHC class I antigen presentation. Front. Immunol. *12*, 636568.
35. Baaten, B.J., Li, C.-R., and Bradley, L.M. (2010). Multifaceted regulation of T cells by CD44. Commun. Integr. Biol. *3*, 508–512.
36. Cibrián, D., and Sánchez-Madrid, F. (2017). CD69: from activation marker to metabolic gatekeeper. Eur. J. Immunol. *47*, 946–953.
37. Ahmadzadeh, M., Johnson, L.A., Heemskerk, B., Wunderlich, J.R., Dudley, M.E., White, D.E., and Rosenberg, S.A. (2009). Tumor antigen–specific CD8 T cells infiltrating the tumor express high levels of PD-1 and are functionally impaired. Blood *114*, 1537–1544.
38. Veglia, F., and Gabrilovich, D.I. (2017). Dendritic cells in cancer: the role revisited. Curr. Opin. Immunol. *45*, 43–51. https://doi.org/10.1016/j.coi.2017.01.002.
39. Chen, B., Khodadoust, M.S., Liu, C.L., Newman, A.M., and Alizadeh, A.A. (2018). Profiling Tumor Infiltrating Immune Cells with CIBERSORT. Methods Mol. Biol. *1711*, 243–259. https://doi.org/10.1007/978-1-4939-7493-1_12.
40. Petitprez, F., Levy, S., Sun, C.M., Meylan, M., Linhard, C., Becht, E., Elarouci, N., Tavel, D., Roumenina, L.T., Ayadi, M., et al. (2020). The murine Microenvironment Cell Population counter method to estimate abundance of tissue-infiltrating immune and stromal cell populations in murine samples using gene expression. Genome Med. *12*, 86. https://doi.org/10.1186/s13073-020-00783-w.
41. Mantovani, A., Allavena, P., Sica, A., and Balkwill, F. (2008). Cancer-related inflammation. Nature *454*, 436–444.
42. Chow, K.T., Gale, M., Jr., and Loo, Y.-M. (2018). RIG-I and other RNA sensors in antiviral immunity. Annu. Rev. Immunol. *36*, 667–694.
43. Reticker-Flynn, N.E., Zhang, W., Belk, J.A., Basto, P.A., Escalante, N.K., Pilarowski, G.O.W., Bejnood, A., Martins, M.M., Kenkel, J.A., Linde, I.L., et al. (2022). Lymph node colonization induces tumor-immune tolerance to promote distant metastasis. Cell *185*, 1924–1942.e23. https://doi.org/10.1016/j.cell.2022.04.019.
44. Ottina, E., Levy, P., Eksmond, U., Merkenschlager, J., Young, G.R., Roels, J., Stoye, J.P., Tüting, T., Calado, D.P., and Kassiotis, G. (2018). Restoration of Endogenous Retrovirus Infectivity Impacts Mouse Cancer Models. Cancer Immunol. Res. *6*, 1292–1300. https://doi.org/10.1158/2326-6066.CIR-18-0038.
45. Attig, J., Young, G.R., Stoye, J.P., and Kassiotis, G. (2017). Physiological and Pathological Transcriptional Activation of Endogenous Retroelements Assessed by RNA-Sequencing of B Lymphocytes. Front. Microbiol. *8*, 2489. https://doi.org/10.3389/fmicb.2017.02489.
46. Lindholm, H.T., Chen, R., and De Carvalho, D.D. (2023). Endogenous retroelements as alarms for disruptions to cellular homeostasis. Trends Cancer *9*, 55–68. https://doi.org/10.1016/j.trecan.2022.09.001.
47. Harding, J., Vintersten-Nagy, K., Yang, H., Tang, J.K., Shutova, M., Jong, E.D., Lee, J.H., Massumi, M., Oussenko, T., Izadifar, Z., et al. (2024). Immune-privileged tissues formed from immunologically cloaked mouse embryonic stem cells survive long term in allogeneic hosts. Nat. Biomed. Eng. *8*, 427–442. https://doi.org/10.1038/s41551-023-01133-y.
48. Braud, V.M., Allan, D.S., and McMichael, A.J. (1999). Functions of nonclassical MHC and non-MHC-encoded class I molecules. Curr. Opin. Immunol. *11*, 100–108.
49. Kovats, S., Main, E.K., Librach, C., Stubblebine, M., Fisher, S.J., and DeMars, R. (1990). A class I antigen, HLA-G, expressed in human trophoblasts. Science *248*, 220–223.
50. Wang, C., Li, Y., Jia, L., Kim, J.K., Li, J., Deng, P., Zhang, W., Krebsbach, P.H., and Wang, C.-Y. (2021). CD276 expression enables squamous cell carcinoma stem cells to evade immune surveillance. Cell Stem Cell *28*, 1597–1613.e7.
51. Liu, S., Liang, J., Liu, Z., Zhang, C., Wang, Y., Watson, A.H., Zhou, C., Zhang, F., Wu, K., Zhang, F., et al. (2021). The role of CD276 in cancers. Front. Oncol. *11*, 654684.
52. Sheng, H., Dasgupta, S., and Kumar, V.C. (2021). Involvement of Qa-1/HLA-E-Restricted CD8+ T Cells in Anti-Microbe and Anti-Cancer Immunity as Well as in Immune Regulation. Crit. Rev. Immunol. *41*, 39–53. https://doi.org/10.1615/CritRevImmunol.2021040144.
53. Borst, L., van der Burg, S.H., and van Hall, T. (2020). The NKG2A-HLA-E Axis as a Novel Checkpoint in the Tumor Microenvironment. Clin. Cancer Res. *26*, 5549–5556. https://doi.org/10.1158/1078-0432.CCR-19-2095.
54. Mu, X., Ahmad, S., and Hur, S. (2016). Endogenous retroelements and the host innate immune sensors. Adv. Immunol. *132*, 47–69.
55. Rehwinkel, J., and Gack, M.U. (2020). RIG-I-like receptors: their regulation and roles in RNA sensing. Nat. Rev. Immunol. *20*, 537–551.
56. Liu, D., Schilling, B., Liu, D., Sucker, A., Livingstone, E., Jerby-Arnon, L., Zimmer, L., Gutzmer, R., Satzger, I., Loquai, C., et al. (2019). Integrative molecular and clinical modeling of clinical outcomes to PD1 blockade in patients with metastatic melanoma. Nat. Med. *25*, 1916–1927. https://doi.org/10.1038/s41591-019-0654-5.
57. Chiappinelli, K.B., Strissel, P.L., Desrichard, A., Li, H., Henke, C., Akman, B., Hein, A., Rote, N.S., Cope, L.M., Snyder, A., et al. (2015). Inhibiting DNA Methylation Causes an Interferon Response in Cancer via dsRNA Including Endogenous Retroviruses. Cell *162*, 974–986. https://doi.org/10.1016/j.cell.2015.07.011.
58. Roulois, D., Loo Yau, H., Singhania, R., Wang, Y., Danesh, A., Shen, S.Y., Han, H., Liang, G., Jones, P.A., Pugh, T.J., et al. (2015). DNA-Demethylating Agents Target Colorectal Cancer Cells by Inducing Viral Mimicry by Endogenous Transcripts. Cell *162*, 961–973. https://doi.org/10.1016/j.cell.2015.07.056.
59. Topper, M.J., Vaz, M., Chiappinelli, K.B., DeStefano Shields, C.E., Niknafs, N., Yen, R.W.C., Wenzel, A., Hicks, J., Ballew, M., Stone, M., et al. (2017). Epigenetic Therapy Ties MYC Depletion to Reversing Immune Evasion and Treating Lung Cancer. Cell *171*, 1284–1300.e21. https://doi.org/10.1016/j.cell.2017.10.022.

60. Sheng, W., LaFleur, M.W., Nguyen, T.H., Chen, S., Chakravarthy, A., Conway, J.R., Li, Y., Chen, H., Yang, H., Hsu, P.H., et al. (2018). LSD1 Ablation Stimulates Anti-tumor Immunity and Enables Checkpoint Blockade. Cell *174*, 549–563.e19. https://doi.org/10.1016/j.cell.2018.05.052.

61. Zhang, S.M., Cai, W.L., Liu, X., Thakral, D., Luo, J., Chan, L.H., McGeary, M.K., Song, E., Blenman, K.R.M., Micevic, G., et al. (2021). KDM5B promotes immune evasion by recruiting SETDB1 to silence retroelements. Nature *598*, 682–687. https://doi.org/10.1038/s41586-021-03994-2.

62. Jung, H., Kim, H.S., Kim, J.Y., Sun, J.M., Ahn, J.S., Ahn, M.J., Park, K., Esteller, M., Lee, S.H., and Choi, J.K. (2019). DNA methylation loss promotes immune evasion of tumours with high mutation and copy number load. Nat. Commun. *10*, 4278. https://doi.org/10.1038/s41467-019-12159-9.

63. Han, Y., Liu, D., and Li, L. (2020). PD-1/PD-L1 pathway: current researches in cancer. Am. J. Cancer Res. *10*, 727–742.

64. Garcia-Diaz, A., Shin, D.S., Moreno, B.H., Saco, J., Escuin-Ordinas, H., Rodriguez, G.A., Zaretsky, J.M., Sun, L., Hugo, W., Wang, X., et al. (2017). Interferon receptor signaling pathways regulating PD-L1 and PD-L2 expression. Cell Rep. *19*, 1189–1201.

65. Gobin, S.J., and van den Elsen, P.J. (2000). Transcriptional regulation of the MHC class ib genes HLA-E, HLA-F, and HLA-G. Hum. Immunol. *61*, 1102–1107.

66. Xiang, X., Wang, J., Lu, D., and Xu, X. (2021). Targeting tumor-associated macrophages to synergize tumor immunotherapy. Signal Transduct. Target. Ther. *6*, 75.

67. Ness, S., Lin, S., and Gordon, J.R. (2021). Regulatory dendritic cells, T cell tolerance, and dendritic cell therapy for immunologic disease. Front. Immunol. *12*, 633436.

68. Podestà, M.A., Cucchiari, D., and Ponticelli, C. (2015). The diverging roles of dendritic cells in kidney allotransplantation. Transplant. Rev. *29*, 114–120.

69. Ribas, A. (2015). Adaptive Immune Resistance: How Cancer Protects from Immune Attack. Cancer Discov. *5*, 915–919. https://doi.org/10.1158/2159-8290.CD-15-0563.

70. McGranahan, N., Rosenthal, R., Hiley, C.T., Rowan, A.J., Watkins, T.B.K., Wilson, G.A., Birkbak, N.J., Veeriah, S., Van Loo, P., Herrero, J., et al. (2017). Allele-Specific HLA Loss and Immune Escape in Lung Cancer Evolution. Cell *171*, 1259–1271.e11. https://doi.org/10.1016/j.cell.2017.10.001.

71. Murgia, C., Pritchard, J.K., Kim, S.Y., Fassati, A., and Weiss, R.A. (2006). Clonal origin and evolution of a transmissible cancer. Cell *126*, 477–487.

72. Caldwell, A., Coleby, R., Tovar, C., Stammnitz, M.R., Kwon, Y.M., Owen, R.S., Tringides, M., Murchison, E.P., Skjødt, K., Thomas, G.J., et al. (2018). The newly-arisen Devil facial tumour disease 2 (DFT2) reveals a mechanism for the emergence of a contagious cancer. eLife *7*, e35314. https://doi.org/10.7554/eLife.35314.

73. Sunderland, C.A., Sasagawa, M., Kanazawa, K., Stirrat, G.M., and Takeuchi, S. (1985). An immunohistological study of HLA antigen expression by gestational choriocarcinoma. Br. J. Cancer *51*, 809–814.

74. Inaguma, S., Wang, Z., Lasota, J., Sarlomo-Rikala, M., McCue, P.A., Ikeda, H., and Miettinen, M. (2016). Comprehensive immunohistochemical study of programmed cell death ligand 1 (PD-L1): analysis in 5536 cases revealed consistent expression in trophoblastic tumors. Am. J. Surg. Pathol. *40*, 1133–1142.

75. Singer, G., Kurman, R.J., McMaster, M.T., and Shih, I.-M. (2002). HLA-G immunoreactivity is specific for intermediate trophoblast in gestational trophoblastic disease and can serve as a useful marker in differential diagnosis. Am. J. Surg. Pathol. *26*, 914–920.

76. Rinke de Wit, T.F., Vloemans, S., van den Elsen, P.J., Haworth, A., and Stern, P.L. (1990). Differential expression of the HLA class I multigene family by human embryonal carcinoma and choriocarcinoma cell lines. J. Immunol.: 1950 *144*, 1080–1087.

77. Ghorani, E., Kaur, B., Fisher, R.A., Short, D., Joneborg, U., Carlson, J.W., Akarca, A., Marafioti, T., Quezada, S.A., Sarwar, N., and Seckl, M.J. (2017). Pembrolizumab is effective for drug-resistant gestational trophoblastic neoplasia. Lancet *390*, 2343–2345.

78. Andre, P., Denis, C., Soulas, C., Bourbon-Caillet, C., Lopez, J., Arnoux, T., Blery, M., Bonnafous, C., Gauthier, L., Morel, A., et al. (2018). Anti-NKG2A mAb Is a Checkpoint Inhibitor that Promotes Anti-tumor Immunity by Unleashing Both T and NK Cells. Cell *175*, 1731–1743.e1713. https://doi.org/10.1016/j.cell.2018.10.014.

79. Tinker, A.V., Hirte, H.W., Provencher, D., Butler, M., Ritter, H., Tu, D., Azim, H.A., Jr., Paralejas, P., Grenier, N., Hahn, S.A., et al. (2019). Dose-Ranging and Cohort-Expansion Study of Monalizumab (IPH2201) in Patients with Advanced Gynecologic Malignancies: A Trial of the Canadian Cancer Trials Group (CCTG): IND221. Clin. Cancer Res. *25*, 6052–6060. https://doi.org/10.1158/1078-0432.CCR-19-0298.

80. Strong, L.C. (1922). A genetic analysis of the factors underlying susceptibility to transplantable tumors (Columbia University).Journal of Experimental. Zoology *36*, 66–134.

81. Quintana, E., Shackleton, M., Sabel, M.S., Fullen, D.R., Johnson, T.M., and Morrison, S.J. (2008). Efficient tumour formation by single human melanoma cells. Nature *456*, 593–598. https://doi.org/10.1038/nature07567.

82. Zhyvoloup, A., Melamed, A., Anderson, I., Planas, D., Lee, C.H., Kriston-Vizi, J., Ketteler, R., Merritt, A., Routy, J.P., Ancuta, P., et al. (2017). Digoxin reveals a functional connection between HIV-1 integration preference and T-cell activation. PLoS Pathog. *13*, e1006460. https://doi.org/10.1371/journal.ppat.1006460.

83. Kim, D., Paggi, J.M., Park, C., Bennett, C., and Salzberg, S.L. (2019). Graph-based genome alignment and genotyping with HISAT2 and HISAT-genotype. Nat. Biotechnol. *37*, 907–915. https://doi.org/10.1038/s41587-019-0201-4.

84. Pertea, M., Pertea, G.M., Antonescu, C.M., Chang, T.C., Mendell, J.T., and Salzberg, S.L. (2015). StringTie enables improved reconstruction of a transcriptome from RNA-seq reads. Nat. Biotechnol. *33*, 290–295. https://doi.org/10.1038/nbt.3122.

85. Liao, Y., Smyth, G.K., and Shi, W. (2014). featureCounts: an efficient general purpose program for assigning sequence reads to genomic features. Bioinformatics *30*, 923–930. https://doi.org/10.1093/bioinformatics/btt656.

86. Quinlan, A.R., and Hall, I.M. (2010). BEDTools: a flexible suite of utilities for comparing genomic features. Bioinformatics *26*, 841–842. https://doi.org/10.1093/bioinformatics/btq033.

87. Love, M.I., Huber, W., and Anders, S. (2014). Moderated estimation of fold change and dispersion for RNA-seq data with DESeq2. Genome Biol. *15*, 550. https://doi.org/10.1186/s13059-014-0550-8.

88. Subramanian, A., Tamayo, P., Mootha, V.K., Mukherjee, S., Ebert, B.L., Gillette, M.A., Paulovich, A., Pomeroy, S.L., Golub, T.R., Lander, E.S., and Mesirov, J.P. (2005). Gene set enrichment analysis: a knowledge-based approach for interpreting genome-wide expression profiles. Proc. Natl. Acad. Sci. USA *102*, 15545–15550. https://doi.org/10.1073/pnas.0506580102.

89. Wheeler, T.J., and Eddy, S.R. (2013). nhmmer: DNA homology search with profile HMMs. Bioinformatics *29*, 2487–2489. https://doi.org/10.1093/bioinformatics/btt403.

90. Kim, D., Langmead, B., and Salzberg, S.L. (2015). HISAT: a fast spliced aligner with low memory requirements. Nat. Methods *12*, 357–360. https://doi.org/10.1038/nmeth.3317.

91. Gao, J., Aksoy, B.A., Dogrusoz, U., Dresdner, G., Gross, B., Sumer, S.O., Sun, Y., Jacobsen, A., Sinha, R., Larsson, E., et al. (2013). Integrative analysis of complex cancer genomics and clinical profiles using the cBioPortal. Sci. Signal. *6*, pl1. https://doi.org/10.1126/scisignal.2004088.

STAR★METHODS

KEY RESOURCES TABLE

REAGENT or RESOURCE	SOURCE	IDENTIFIER
Antibodies		
Anti-mouse H-2Db (PerCP/Cy5.5)	Biolegend	RRID: AB_2565865
Anti-mouse H-2Kb (Pacific Blue)	Biolegend	RRID: AB_1967103
Anti-mouse CD274/PD-L1 (PE)	Biolegend	RRID: AB_2073557
Anti-mouse Qa-1(b) (BV510)	BD Biosciences	RRID: AB_2742199
Anti-mouse CD45 (BV421)	BD Biosciences	RRID: AB_2651151
Anti-mouse CD3 (APC)	Invitrogen	RRID: AB_1907372
Anti-mouse Npk46 (PE)	Invitrogen	RRID: AB_1210743
Anti-mouse CD4 (FITC)	Biolegend	RRID: AB_312690
Anti-mouse CD8a (BUV805)	BD Biosciences	RRID: AB_2870186
Anti-mouse Gr-1/Ly-6G (BV510)	Biolegend	RRID: AB_2562214
Anti-mouse CD11b (BV711)	Biolegend	RRID: AB_11218791
Anti-mouse F4/80 (APC-eFluor)	Biolegend	RRID: AB_2735036
Anti-mouse MHC II (I-A/I-E)	Invitrogen	RRID: AB_494009
Anti-mouse CD11c (PE/Cy7)	Biolegend	RRID: AB_493569
Anti-mouse CD45 (Alexa Fluor 700)	Biolegend	RRID: AB_493714
Anti-mouse CD3e (BUV395)	BD Biosciences	RRID: AB_2738278
Anti-mouse CD4 (PerCP/Cy5.5)	Biolegend	RRID: AB_893330
Anti-mouse CD44 (APC)	Biolegend	RRID: AB_312962
Anti-mouse CD69 (APCeFluor780)	Biolegend	RRID: AB_492844
Anti-mouse PD-1	Biolegend	RRID: AB_312962
InVivoPlus anti-mouse PD-1	Bio X Cell	RRID: AB_10949053
InVivo Mab anti-mouse Qa-1b	Bio X Cell	RRID: AB_10949623
InVivoPlus mouse IgG1 isotype control	Bio X Cell	RRID: AB_1107784
Bacterial and virus strains		
One Shot™ Stbl3™ Chemically Competent E. coli	Invitrogen	C737303
eSpCas9-LentiCRISPR v2	Genscript	SC1678
Chemicals, peptides, and recombinant proteins		
Collagenase IV	Sigma-Aldrich	C-28-100MG
DNAseI	Roche	10104159001
Critical commercial assays		
Mouse CXCL10/IP-10/CRG-2	R&Dsystems	DY466-05
Mouse CCL5/RANTES	R&Dsystems	DY478-05
RNAeasy kit	Qiagen	74104
Deposited data		
YUMM cells RNAseq (all passages)	GEO	GSE288825
Tumor biopsies YUMM RNAseq	GEO	GSE288897
Tumor biopsies human melanoma	dbGaP	Phs000452.v3.p1 (https://www.ncbi.nlm.nih.gov/projects/gap/cgi-bin/study.cgi?study_id=phs000452.v3.p1)
Code	GitHub	https://github.com/secrierlab/Metastatic-melanoma-anti-PD1/

(*Continued on next page*)

Continued

REAGENT or RESOURCE	SOURCE	IDENTIFIER
Experimental models: Cell lines		
YUMM1.7 cells	ATCC	CRL-3362
YUMM1.7 passages (F0, F1, F2, N2.1, N2.2, N2.3, Balb-*c*-1, Balb/c-2, CBA, FVB/N)	This study	–
Experimental models: Organisms/strains		
6-8 weeks old inbred male and female Mouse/C57BL/6	Charles River and Envigo	N/A
6-8 weeks old inbred male and female Mouse/BALB/c	Charles River and Envigo	N/A
6-8 weeks old inbred male and female Mouse/CBA/Ca	Envigo	N/A
6-8 weeks old inbred male and female Mouse/FVB/N	Envigo	N/A
6-8 weeks old inbred male and female Mouse/C57BL/6	Charles River and Envigo	N/A
6-8 weeks old inbred male and female Mouse/BALB/c	Charles River and Envigo	N/A
Oligonucleotides		
gRNA1 Ddx58 (F: ATA CCG CTT CCA CAA AAG CT)	Thermo Fisher Scientific	N/A
gRNA1 Ddx58 (R: CCA TGT AGT TCC CTT CCT CC)	Thermo Fisher Scientific	N/A
gRNA 2 Ddx58 (F: AAG CCA TCG AAA GTT GGG AC)	Thermo Fisher Scientific	N/A
gRNA 2 Ddx58 (R: AAG GGG GCA ACT TTA ACT GC)	Thermo Fisher Scientific	N/A
Beta Actin (F: TGA GCT GCG TTT TAC ACC CT)	Thermo Fisher Scientific	N/A
Beta Actin (R: AAG TCA GTG TAC AGG CCA GC)	Thermo Fisher Scientific	N/A
Software and algorithms		
FlowJo-v10	FlowJo LLC	N/A
Prism Graphpad 10	Graphpad	N/A
Biorender	Biorender	N/A
Gene Set Enrichment Analysis v4.1.0	UC San Diego, Broad Institute	N/A
Stringtie v1.3.3b (transcript assembly)	https://ccb.jhu.edu/software/stringtie/	–
FeatureCounts v1.5.0-p3 (gene counts)	https://bioconductor.org/packages/release/bioc/html/Rsubread.html	–
QIAGEN IPA (pathway analysis)	https://digitalinsights.qiagen.com/products-overview/discovery-insights-portfolio/analysis-and-visualization/qiagen-ipa/?cmpid=QDI_GA_DISC_IPA&gad_source=1	–
RepeatMasker v.4.09 (analysis of repeats)	www.repeatmasker.org	–
Qlucore Omics Explorer 3.3 (repeat expression analysis)	www.qlucore.com	–
GFFUtils gtf2bed (repeats mapping)	github.com/fls-bioinformatics-core/GFFUtils	–
DESeq2 v1.32.0 (differential gene expression)	https://bioconductor.org/packages/release/bioc/html/DESeq2.html	–
BioMart R	https://www.ensembl.org/info/data/biomart/index.html	–
Survminer R	https://www.sthda.com/english/wiki/survminer-r-package-survival-data-analysis-and-visualization	–
Survival R	https://doi.org/10.32614/CRAN.package.survival	–
Ggpubr R	https://doi.org/10.32614/CRAN.package.ggpubr	–

EXPERIMENTAL MODEL AND STUDY PARTICIPANT DETAILS

Human samples

The human melanoma dataset profiling samples before and after treatment with anti-PD1 antibodies was sourced from Li et al. (https://pubmed.ncbi.nlm.nih.gov/31792460/) and downloaded from cBioportal. Raw sequencing data from the study are publicly

available in dbGaP (accession number phs000452.v3.p1). RNA-seq and matched clinical data were available for n = 121 patients (50 females, 71 males). Ancestry, gender and ethnicity were not reported in the original study. Samples were split into groups based on the presence/absence of a Balb/c-2 signature (see Quantification and Statistical Analyses). Sex did not have an impact on survival outcomes when modeling group effects with Cox proportional hazards models.

Animal experiments

All experiments with mice, handling and euthanasia were performed in accordance with UK Home Office regulations, project license number PP2330953 and number PC79FA7AB under study approval and supervision from the Biological Safety Unit at UCL in accordance with the 3R (Replacement, Reduction, Refinement) Principles. 6–8 weeks old inbred C57BL/6J and BALB/c mice were acquired from Charles River and Envigo, CBA/Ca and FVB/N mice were acquired from Envigo. Mice were maintained in conventional colonies and housed in individually ventilated cages. Mice health was monitored daily for general signs of health, including activity, appearance, weight loss, clinical signs such as diarrhea and dehydration, and whether there were changes to the mouse body condition i.e.,: apparent skeletal structure changes or loss of muscles before and after tumor injections. For breeding, 2 males and 2 females' breeders were set to get litters for the required mouse strains or hybrids: F1 (C57BL/6 x BALB/c), F2 (F1 x F1) and N2 (F2 x BALB/c). 6–8 weeks old male and female mice were randomized for tumor implantation studies in equal ratios. The experimental set up and data analysis were not designed to detect sex-specific effects because tumor allograft rejection is observed at equal rates in adult male and female mice.[11–13,80] Mouse genotyping was done using the Mini Mouse Universal Genotyping Array (MUGA) platform by Transnetyx on spleen cells (Table S1).

Tumor cell transplantation

Tumor cells were grown *in-vitro* for 2 to a maximum of 4 passages. Cells were suspended in sterile PBS at 10 million cells/ml and prepared for injection. Mice were anesthetized, weighted, ear clipped, shaved at the site of injection and injected in the left flank area with 1 million cells in 100 μL PBS. Mice were monitored daily for tumor growth and their general health was assessed using the BSU scoring system. Mice weights were monitored and recorded on a bi-daily basis. Tumors were measured by a caliper at regular intervals and when tumors reached 15mm in diameter, the mice were culled, and tumors and spleens were collected for analysis.

In-vivo neutralizing antibodies treatment

Mice were injected in the left flank with 1 million Balb/c-2 tumor cells in 100 μL sterile PBS. After tumors became palpable, mice weights were measured, and mice were injected intraperitoneally with antibodies (5mg/Kg) every three days for 4 times. Mice were monitored daily, and tumor volumes recorded. Mice were injected with the following neutralizing antibodies: Anti mouse PD-1 (RMP1-14, BioXcell), anti-mouse Qa-1b (4C2.4A7.5H11, BioXcell), and mouse IgG1 isotype control (MOPC-21, BioXcell) were prepared in pH 7.0 Dilution Buffer (bioXcell).

Cell lines

Parental YUMM1.7 were obtained from the American Tissue Culture Collection (CRL-3362). They are derived from an adult male C57BL/6 mouse with $Braf^{V600E}$/wt (knock in conditionally activated Braf allele), $Cdkn2a^{-/-}$ $Pten^{-/-}$ (conditionally inactivated) and the Tyrosinase:CreERT2 transgene. YUMM1.7 and dissociated tumor cells were grown in DMEM F-12 media (Gibco) supplemented with 10% FBS (Labtech), 1% non-essential amino acids (Gibco), and 1% penicillin/streptomycin (Gibco). Cells were passaged every 2–3 days at 70–80% confluency. Cell lines were authenticated by genotyping using the Mini Mouse Universal Genotyping Array (MUGA) platform by Transnetyx (Table S1). The cell lines were regularly tested for mycoplasma contamination.

METHOD DETAILS

Tumor and spleen dissociation

The tumor dissociation methods has been previously described.[81] Tumors were dipped in 70% ethanol very briefly and then rinsed in Hank's buffer (HSS) + pen/strep. In a bijou, tumors were minced on ice for 10 min with two pairs of small scissors into small pieces (1 mm or less) in 1mL Hank's buffer +200U/ml Collagenase IV + pen/strep (filter sterilised). After DNAseI addition (1 mg/mL final), the samples were incubated for 25 min at 37^0C with gentle shaking. Samples were washed in 10 mL cold Hank's buffer, digested with 1 mL of 0.05% Trypsin-EDTA for 5 min at 37^0C and filtered through a 70 μm nylon mesh adding HSS to prevent clogging. Samples were diluted in 30 mL HSS + pen/strep, centrifuged at 1,500 rpm in a benchtop centrifuge for 5 min and resuspend in the appropriate buffer. Mouse spleens were filtered through a 70 μm nylon mesh, then RBCs were lysed using RBC Lysis Buffer (Biolegend). Cells were washed then resuspended in FACS buffer.

In-vitro cell surface staining and flow cytometry

Cells were grown in media until around 100% confluent. Then cells were washed, trypsinised and centrifugated. Cells were resuspended in FACS buffer and aliquoted in FACS tubes. For *ex vivo* staining: dissociated tumor cells were resuspended in FACS buffer and aliquoted in FACS tubes. For *in vitro* staining: cells were stained with the following antibodies: H2Db (PerCP/Cy5.5, Biolegend), H2Kb (Pacific Blue, Biolegend), PD-L1 (PE, Biolegend) and Qa-1(b) (BV510, BD Bioscience). For *ex vivo* staining dissociated cells

were stained with the following antibodies: CD45 (BV421, BD Bioscience), CD3 (APC, Invitrogen), NKp46 (PE, Invitrogen), CD4 (FITC, Biolegend) CD8α (BUV805, BD Bioscience), Gr-1 (BV510, Biolegend), CD11b (BV711, Biolegend), F4/80 (APC-eFlour780, Invitrogen), MHC II (I-A/I-E) (Alexa Flour 700, Invitrogen), CD11c (PE/Cy7, Biolegend), CD45 (Alexa Flour 700, Biolegend), CD3 (BUV395, BD Bioscience), CD4 (PerCP/Cy5.5, Biolegend), CD44 (APC, Biolegend), CD69 (APC-eFlour780, Biolegend), PD-1 (BV711, Biolegend), and Live/Dead (live dead blue, ThermoFisher). Antibodies were diluted 1:100 in FACS buffer containing the cells and incubated for 30 min at 4°C in the dark. Cells were washed with 2 mL PBS, resuspended in 200 μL FACS buffer +200 μL 4% paraformaldehyde (PFA) and analyzed using BD Fortessa flow cytometers. Absolute count was calculated using CountBright Absolute counting Beads (Invitrogen) following the manufacturer instructions. To assist with gating in the 16-color panel, fluorescence minus one control was used, then the gating strategy obtained from FMO was applied on *ex vivo* tumor samples. The gating method to identify population of cells was created by comparing stains with and without a certain antibody.

In-vitro intracellular MHC-I staining

Cells were grown in media until around 100% confluent. Then cells were washed in PBS, trypsinised and centrifugated. Cells were fixed in 500 μL fixation buffer for 20 min at room temperature in the dark. Cells were centrifugated at 350X g for 5 min and resuspended in 200 μL permeabilization/wash buffer, then centrifugated at 350X g for 5 min. Supernatant was decanted, cells were resuspended in 200 μL prem/wash buffer and centrifugated at 350X g for 5 min. After decanting the supernatant, the cells were stained with the antibodies at 1:100 dilution in the permeabilization/wash buffer and incubated for 20 min in the dark at 4°C. Cells were washed 2 times with perm/wash buffer and centrifugated at 350X g for 5 min. Cells were resuspended in 200 μL FACS buffer and analyzed using BD Fortessa flow cytometers.

Fluorescent ICC staining

Cells were grown in media on top of a coverslip coated with 0.1% gelatin. Then cells were washed with PBS. Cells were stained with H2Db (1:100, Biolegend) and Concanavalin A (50 μg/mL, Invitrogen) for 30 min in the dark at room temperature. Cells were washed the fixed with 4% paraformaldehyde. Coverslips were transferred to slides on top of nuclear stain with mounting media (DAPI, Invitrogen). Slides were imaged on Nikon C2 confocal microscope.

RIG-I KO by Crispr/Cas9

To produce Rig-I KO Balb/c-2 cells, 293T cells were transfected using FuGENE transfection reagent with 3 plasmids 1- eSpCas9-LentiCRISPR v2 with gRNAs targeting *Ddx58* gene (gRNA1: ATGTCTTATCAGATCCGACA, gRNA2: ATCCGAATGTTTGATTAATC) or Empty vector (GenScript). 2- pCMV-VSV-G envelope. 3- and pCMV-Gag/Pol packaging vectors as previously described.[82] After 24 h, media was changed. The virus-containing supernatants were collected 48 and 72 h after transfection. Balb/c-2 cells were infected with the lentivirus in the presence of 8 μg/mL Polybrene. Forty-eight hours after infection, fresh media containing puromycin (2 μg/mL) was added and clones were selected by limiting dilution. DNA was extracted from different clones and control samples using phenol/chloroform. PCR amplification was performed with the following primers: gRNA1 *Ddx58* (F: ATA CCG CTT CCA CAA AAG CT, R: CCA TGT AGT TCC CTT CCT CC) gRNA 2 *Ddx58* (F: AAG CCA TCG AAA GTT GGG AC, R: AAG GGG GCA ACT TTA ACT GC) Beta Actin (F: TGA GCT GCG TTT TAC ACC CT, R: AAG TCA GTG TAC AGG CCA GC).

ELISA

Tumor cells were grown *in-vitro* in 6 well plates until almost 100% confluent. Supernatant was collected, then centrifugated briefly to remove debris and CXCL10 and CCL5 were detected using the solid phase sandwich Quantikine ELISA R&D systems kit according to the manufacturer's instructions. Optical density was determined by using a microplate reader at 450nm (Thermo Scientific).

In-vivo neutralizing antibodies treatment

Mice were injected in the left flank with 1 million Balb/c-2 tumor cells in 100 μL sterile PBS. After tumors became palpable, mice weights were measured, and mice were injected intraperitoneally with antibodies (5mg/Kg) every three days for 4 times. Mice were monitored daily, and tumor volumes recorded. Mice were injected with the following neutralizing antibodies: Anti mouse PD-1 (RMP1-14, BioXcell), anti-mouse Qa-1b (4C2.4A7.5H11, BioXcell), and mouse IgG1 isotype control (MOPC-21, BioXcell) were prepared in pH 7.0 Dilution Buffer (bioXcell).

RNA extraction

Total RNA was extracted using the RNAeasy kit following the manufacturer's instructions. Briefly, cells were trypsinised and washed with PBS. Biopsies and cells were lysed with RLT buffer until totally homogenized. 1 volume of 70% ethanol was added, and the lysate was mixed and moved to the Rneasy spin column and centrifugated. The Flowthrough was discarded. The column was washed with RW buffer, then RPE buffer twice. RNA was eluted with nuclease free water and stored at −80°C.

Library preparation for transcriptome sequencing

The RNAseq library was prepared by Novogene (Cambridge, UK). Messenger RNA was purified from total RNA using poly-T oligo-attached magnetic beads. After fragmentation, the first strand cDNA was synthesized using random hexamer primers, followed by

the second strand cDNA synthesis using either dUTP for directional library or dTTP for non-directional library. For the non-directional library, it was ready after end repair, A-tailing, adapter ligation, size selection, amplification, and purification for the directional library, it was ready after end repair, A-tailing, adapter ligation, size selection, USER enzyme digestion, amplification, and purification. The library was checked with Qubit and real-time PCR for quantification and bioanalyzer for size distribution detection. Quantified libraries will be pooled and sequenced on Illumina platforms, according to effective library concentration and data amount.

Clustering and sequencing

The clustering of the index-coded samples was performed according to the manufacturer's instructions. After cluster generation, the library preparations were sequenced by Novogene on a NovaSeq platform at 150 bp paired-end reads. Sequences with a Q score $\leq$5 over 50% of the nucleotides or with N > 10% were discarded.

Quality control

Raw data (raw reads) of fastq format were firstly processed through in-house perl scripts. In this step, clean data (clean reads) were obtained by removing reads containing adapter, reads containing ploy-N and low-quality reads from raw data. At the same time, Q20, Q30 and GC content the clean data were calculated. All the downstream analyses were based on the clean data with high quality.

Reads mapping to the reference genome

Sequences were mapped to the mouse transcriptome from build GRCm38 (aka mm10), obtained from Ensembl, using the aligner HiSat2 v2.0.5,[83] assembled into transcripts with Stringtie v1.3.3b,[84] and summarised into gene counts with featureCounts v1.5.0-p3.[85] On average 45 million sequence paired ends were obtained, ranging between 35 and 57 million per sample.

Annotation of intergenic and intragenic repeats

Lists of inter and intragenic repeats were created by analysing the intersection of bed files of gene and repeat loactions. A bed file of gene locations from GRCm38.78 was prepared from the GTF using GFFUtils gtf2bed (github.com/fls-bioinformatics-core/GFFUtils). A second bed file was generated from the GTF of repeats using the same method. The intersection of these bed files was found using BEDtools Intersect.[86] Qlucore annotation text files of lists of gene intersecting and non-gene-intersecting repeats were then made and used to annotate heatmaps. The lists were also used for enrichment analysis in R. Both the chi-squared and fisher's exact test results are reported.

Graphical Illustrations

Graphical Illustrations were performed using Biorender.

QUANTIFICATION AND STATISTICAL ANALYSIS

Phenotypic analysis of the tumor cells

Statistical analysis for samples of more than 3 groups was performed using GraphPad Prism v10 and 1-way Anova or two-way ANOVA with Tukey correction for multiple comparisons, p values of 0.05 or less were considered significant. Statistical analysis for samples of less than 3 groups was carried out using unpaired t test with Welch correction. The statistical details including the statistical tests used and exact value of n are all specified in the figure legends.

Quantification of gene expression level

featureCounts v1.5.0-p3 was used to count the reads numbers mapped to each gene. And then FPKM of each gene was calculated based on the length of the gene and reads count mapped to this gene. FPKM, expected number of Fragments Per Kilobase of transcript sequence per Millions base pairs sequenced, considers the effect of sequencing depth and gene length for the reads count at the same time, and is currently the most commonly used method for estimating gene expression levels.

Differential expression analysis

Normalisation and differential expression analysis was performed with DESeq2 v1.32.0[87] using the raw gene counts as input, with "YUMM17″ as a reference. The function 'lfcShrink' was applied in order to shrink toward zero the logFoldChange of genes with low counts and high variability. Wald test p-values were adjusted for multiple testing using the default Benjamini-Hochberg method, which returns the false discovery rate (FDR). Genes with an FDR below 5% were considered differentially expressed (DE). The log2 (foldchange) values were subjected to k-means hierarchical clustering with k = 6, and the result was displayed as a heatmap using the R package 'pheatmap' v1.0.12 (https://CRAN.R-project.org/package=pheatmap).

Enriched pathway analysis

DE genes from each comparison (each passage against reference YUMM17) were combined, resulting in 7282 genes. The log2FC values were subjected to k-means hierarchical clustering with k = 6, and the result was displayed as a heatmap using the R package 'pheatmap' v1.0.12 (https://CRAN.R-project.org/package=pheatmap). Each row represents one gene. Functional analysis for any

group of genes of interest (clusters, or Balb/c-2 vs. F0) was performed using Gene Set Enrichment Analysis (GSEA)[88] implemented as a Java tool GSEA v4.1.0 (https://www.gsea-msigdb.org/gsea/index.jsp) using normalised counts and the following parameters: 'meandiv' normalisation, geneset permutation, $n = 1000$ permutations per test, metric Signal2Noise, and weighted enrichment statistic. We queried functional genesets at the MSigDB database (https://www.gsea-msigdb.org/gsea/msigdb/index.jsp) based on Gene Ontology terms Kegg and GOBP and identified those with an FDR <5%.

Ingenuity pathway analysis

Significantly differentially expressed genes were used in QIAGEN IPA core analyses. The following details were loaded into the input table describing the outcome of a differential gene expression analysis: Genome ID, the significance of the impact size is described by the mean expression across all samples, the log2 fold change ratio of the gene expression between the two groups, and the P-value/FDR of the differential-expression test between the two groups.

Analysis and quantification of repeats

Repetitive regions were annotated as previously described.[45] In brief, the mouse genome (GRCm38.78) was masked using RepeatMasker (RepeatMasker v.4.09, www.repeatmasker.org) configured with nhmmer[89] in sensitive mode using the Dfam 2.0 library (v150923). RepeatMasker annotates long terminal repeat and internal regions separately, complicating the summation of reads that span these divides. Tabular outputs were therefore parsed to merge adjacent annotations for the same element and to produce a gene transfer format (GTF) file compatible with popular read-counting programs. Read pairs were aligned with HISAT2[90] and primary, stranded mappings were counted with featureCounts (Subread[85] using standard GTF files for annotated genes and the curated RepeatMasker GTF files for repeat regions. For accuracy and to prevent ambiguity, only reads that could be uniquely assigned to a single feature were counted. Those reads remaining were normalized to account for variable sequencing depth between samples, using DESeq2.[87] All downstream differential expression analyses and visualization were carried out using Qlucore Omics Explorer 3.3 (Qlucore). Analysis of repeat expression was performed using the Qlucore Omics Analysis platform (www.qlucore.com). Scores below 0.1 were discarded and the data was logged to base 2. Repeats were filtered using a t test for all samples before N2.1, and all samples after N2.1 inclusive. Filters were set at SD > 0.34, q < 0.05, and fold-change >2. This was used to produce a heatmap, and 3D PCA plot. Repeats passing this threshold were exported from qlucore. R was used to examine the enrichment of repeat families. Fisher's exact tests were used to test for enrichment of repeat families in the up- and down-regulated repeat lists, compared to all repeats in the mouse genome. Benjamini Hochberg correction was applied to the resulting p-values to account for multiple testing. The same list of repeats was also tested for enrichment of inter or intragenic status of the repeats.

Analysis of human anti-PD1 treated human melanoma dataset

RNA-seq profiles of 121 samples from patients with metastatic melanoma before treatment with anti-PD1 and linked clinical data as reported by Liu et al.[56] were downloaded from cBioPortal.[91] The RNA-seq data were TPM transformed and Z score normalised. Out of 121 samples, 47 were treated with Ipilimumab. Mouse gene symbols were mapped to human gene symbols using the *biomaRt* R package. To identify human tumors presenting the pro-inflammatory Balb/c-2 signature, we subtracted the average expression of cluster 2 genes (strongly downregulated) from the average expression of cluster 1 genes (highly upregulated), and samples with resulting values greater than 0 were deemed Balb/c-2 signature positive. Survival analysis, including Cox proportional hazards modeling, was performed using the *survival* and *survminer* R packages and Kaplan-Meier curves were generated using the *ggpubr* R package.